Energy Reports 7 (2021) 5815–5833

Contents lists available at ScienceDirect

Energy Reports

journal homepage: www.elsevier.com/locate/egyr

Research paper

Enhanced control technique for a sensor-less wind driven doubly fed induction generator for energy conversion purpose

Mahmoud A. Mossa [a], Hamdi Echeikh [b], Atif Iqbal [c,*]

[a] Electrical Engineering Department Faculty of Engineering, Minia University, Minia, 61111, Egypt
[b] Electrical Engineering Department, National Engineering School of Monastir, 5035, Tunisia
[c] Department of Electrical Engineering, Qatar University, Doha, 2713, Qatar

ARTICLE INFO

Article history:
Received 20 April 2021
Received in revised form 11 July 2021
Accepted 25 August 2021
Available online 15 September 2021

Keywords:
Wind energy
Power angle
Predictive control
MPPT
DFIG
Observer

ABSTRACT

The current paper is concerned with introducing a predictive polar flux control (PPFC) scheme for a variable speed wind driven doubly fed induction generator (DFIG) without speed sensor. The operation of the designed PPFC is based on the power angle regulation. The adaptation process is performed through studying the relation between the generator's torque and the power angle between the stator and rotor flux vectors. A robust observer is designed based on the back-stepping theory to estimate the rotor speed, stator currents, rotor flux and stator and rotor resistances. Furthermore, an effective maximum power point tracking (MPPT) scheme is designed to achieve the optimal wind power exploitation. To recognize the operation of the schemed PPFC, a discursive performance evaluation is performed for the modeled control scheme and the classic predictive torque control (PTC) scheme. The achieved results report that the DFIG's performance is effectively enhanced with the proposed PPFC in comparison with the PTC technique. The improved dynamics are observed through the ripples reduction and reduced switching frequency. In addition, the designed observer has successfully managed in estimating the specified variables with high precision.

1. Introduction

Recently, the generation of electricity using renewable energy sources such as wind, solar and geothermal energies is given a great concern due to their several merits compared with traditional ways of generation (Koraki and Strunz, 2018; Zeng et al., 2014; Du et al., 2018; Williamson et al., 2001). Majority of related researches about such systems are focused on solar and wind types, with which several control approaches were proposed to achieve the optimal exploitation of extracted power (Puchalapalli et al., 2020; Kumar et al., 2017; Chishti et al., 2019). For any wind turbine based generation system, the most important item is the optimal control of generation unit. The unit can be of several types such as synchronous generator, self-excited induction generator, doubly fed induction generator (DFIG) and so on (Geng et al., 2011; Polinder et al., 2013; Nayanar et al., 2016; Carroll et al., 2015; Zhang et al., 2014). From these types, the DFIG is considered the most preferred one due to its ability to operate at variable wind speed while providing fixed stator voltage and frequency to the electric utility. Moreover, the DFIG usually uses a reduced power rating inverter to control the rotor side in comparison with the other generators (Han et al., 2013; Iacchetti et al., 2015). Another feature of DFIG is the ability to tolerate the faults which contributes in enhancing the system reliability (Xiahou et al., 2018, 2019; Kanjiya et al., 2014).

For this reason, several studies were concerned with the optimal control of DFIG (Pulgar-Painemal, 2019; Rahimi and Parniani, 2010; Karakasis et al., 2019; Taibi et al., 2014), some of them concerned with studying and improving the dynamics (Pulgar-Painemal, 2019; Rahimi and Parniani, 2010), while the others concerned with how to extract maximum power from the wind (Gaamouche et al., 2020; Mendis et al., 2012). Majority of such control techniques were articulated on two main approaches: the field orientation (FOC) and direct power (DPC) or torque (DTC) control (Marques and Sousa, 2012, 2011; Mohseni et al., 2011). The FOC principle used multiple current regulators and co-ordinates transformation, while the direct power/torque controllers used two hysteresis comparators and a look-up table. The FOC principle was implemented in different forms such as stator field orientation (SFO) (Marques and Sousa, 2012), rotor field orientation (RFO) (Mohseni et al., 2011) and air-gap field orientation (AGFO) (Marques and Sousa, 2011).

In addition to the response delay that the PI regulators cause in the system, the controller's complexity due to the need for tuning several PI regulators is considered the main challenge. These

* Corresponding author.
E-mail addresses: mahmoud_a_mossa@mu.edu.eg (M.A. Mossa), hamdi.engineer.nl@gmail.com (H. Echeikh), atif.iqbal@qu.edu.qa (A. Iqbal).

https://doi.org/10.1016/j.egyr.2021.08.183
2352-4847/

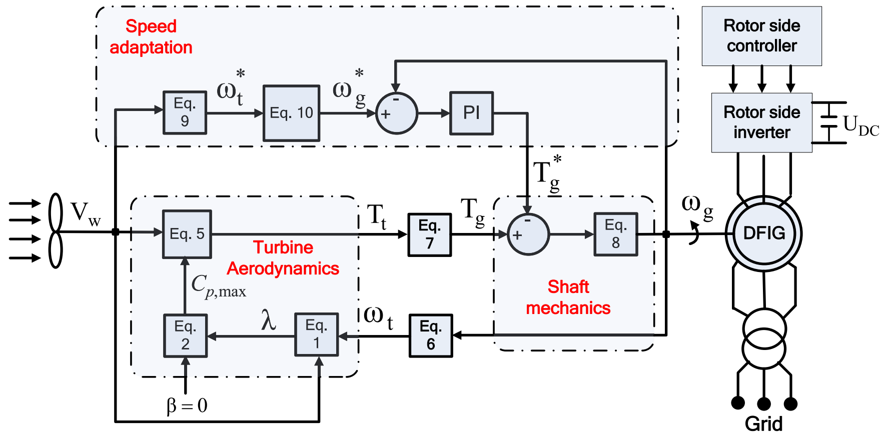

Fig. 1. Wind turbine based energy system.

issues were avoided when adopting the DTC and/or DPC principles. In these control forms, all current regulators are eliminated and replaced by hysteresis regulators besides a designed look-up table for voltage selection purpose (Mondal and Kastha, 2015; Mohammadi et al., 2014). However a faster dynamic is obtained with the hysteresis based controllers, but on the other hand the generator's dynamics are affected by high ripples content. These ripples come in the form of torque pulsations which increase the vibrations in the rotating shaft and can make a severe damage if it is not treated well. The main reason for the accompanied ripples when adopting the DTC or DPC can be referred to the imprecise voltage vectors application, which means that the selected vector during a sampling interval can result in a deviation of the torque/active power or flux/reactive power values.

To avoid the shortages in hysteresis based controllers, the predictive control principle is adopted in the forms of predictive torque control (PTC) and predictive power control (PPC) (Cruz et al., 2018; Abad et al., 2008; Zhang et al., 2020a; Hu et al., 2015). Actually, the PTC can be considered as a mirror or transpose for the PPC and so if one of them is applied, this can accomplish the control targets. In these predictive forms, both hysteresis regulators and look-up tables are avoided and replaced with only one simple cost function which combines the normalized errors of torque and rotor flux as in PTC (Cruz et al., 2018; Abad et al., 2008), and normalized errors of active and reactive power as in PPC (Zhang et al., 2020a; Hu et al., 2015). The main operation of the predictive controllers depend entirely on the minimization of the used cost function, which means that the controller will select the first voltage vector which gives minimum value and then apply it to the machine. From this fact, the voltages selection are performed in two ways when considering the predictive control; the first is through using a PWM technique and this type is called the continuous control set predictive control (CCSPC) (Sguarezi Filho and Filho, 2012; Soliman et al., 2011), while other is performed through selection the voltages directly from a specified set (eight vectors) without using a PWM, and this is entitled with finite control set predictive control (FCSPC) (Gomez et al., 2020; Wei et al., 2019). The CCSPC has the advantage of fixed switching frequency, but on the other hand it has high switching patterns which mean higher pulsations. Meanwhile, the FCSPC has the ability to provide low switching pattern and incorporating the discrete behavior of the voltage source inverter (VSI) in the model, which contributes effectively in making the system response more precise, and for this reason the FCSPC is commonly adopted.

However the dynamic improvement obtained with the predictive control in comparison with the hysteresis control, but predictive control is still suffering from some deficiencies such

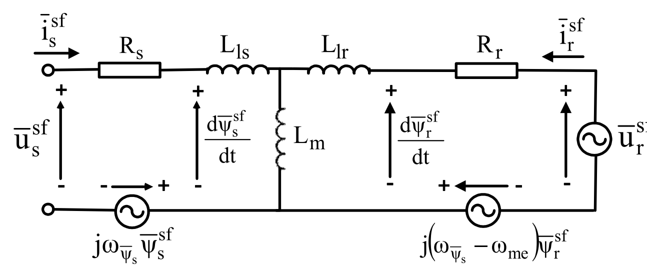

Fig. 2. Circuit model of DFIG in synchronous frame.

as the need to a precise selection of weighting factors (W_f) to be used in cost functions (CF) which have two different error types such as the PTC and PPC. For example in PTC which has a CF consists of the normalized error of torque and rotor flux besides a weighting value multiplied to the flux error in order to balance the weight of errors respecting to each other (Mokhtari Vayeghan and Davari, 2017). Any wrong or in accurate selection of W_f results in deteriorating the dynamics because of the wrong selection of voltage vectors. Another issue related to the predictive control is the calculation time taken to evaluate the CF value in each control loop, which makes a challenge when selecting the microcontroller that can afford the time taken by the controller to execute its operation. A third notice that can be taken about the predictive control is that however the ripples are effectively reduced in comparison with the hysteresis based controllers, but it still present and not totally suppressed. This can be illustrated through analyzing the variation of applied or selected voltage vector; as when an optimal vector is selected by the CF of the controller, this vector is applied along the total sampling period (T_s) until another change in the controller appears. Applying the vector to the entire T_s is not an accurate action, as it may happens that a variation in torque or flux vectors arise within this interval, which finally results in increasing the deviation and thus enlarging the ripples.

To solve some of deficiencies of PTC as a representative of the predictive control, some studies proposed bisecting the sample time so that more than one vector is applied, which contributed in limiting the deviations and ripples but on the other hand the computation time is increased (Zhang et al., 2020b; Zarei et al., 2017). Other studies have concerned with the optimal online selection of the W_f to obtain precise selection of the vectors (Davari et al., 2021), but this also led to an increase in the computation capacity of the controller which cannot usually be sustained by the microprocessors. Other studies adopted the

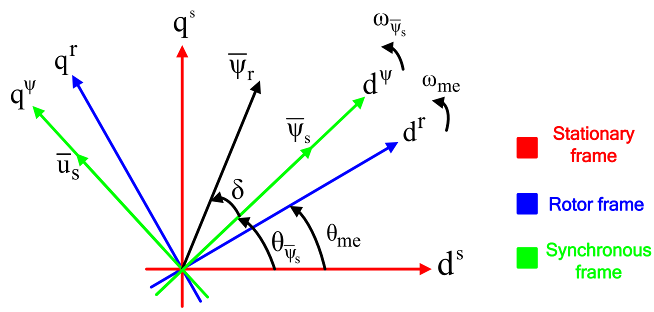

Fig. 3. Displacements of vectors in different co-ordinates.

incorporation of adaptive flux observers to get a smoothed response (Davari and Arab Khburi, 2015; Zebirate et al., 2014), but in the other hand the system complexity is increased.

To keep the balance between the low ripples and the reasonable computation time, this paper proposes an innovative polar predictive flux control (PPFC), in which the cost function is formulated using two error terms with the same type (errors of direct and quadrature components of rotor flux), and thus there is no need to use a weighting value as in PTC schemes. In addition, the proposed PPFC does not utilize any flux adaptation mechanism which saves the computation time within a reduced range compared with the PTC.

To increase the reliability of the wind driven DFIG system, various research studies have concerned with eliminating the mechanical speed sensor and replacing it with an estimation procedure. It is worth realizing that the accuracy of estimating or measuring the speed or position reflects on the performance of the overall control system, and so the precise speed/position estimation is another challenge which is suitably dealt in the current paper.

Generally, the speed estimation techniques are categorized into two procedures: the open loop (OL) estimation procedure (Marques et al., 2013; Karthikeyan et al., 2012; Bhattarai et al., 2018a; Marques and Sousa, 2013), and the closed loop (CL) one (Castelli-Dezza et al., 2013; Bhattarai et al., 2018b; Ajabi-Farshbaf et al., 2017). The OL observers are extracting the rotor position from the difference between the positions of rotor current vector in two reference co-ordinates (mainly the stationary and rotor co-ordinates). Meanwhile, the CL observers usually utilize reduce or full order estimators. Some of these observers are presented in (You et al., 2018) in the form of Luenberger observer, in (Yin et al., 2019) in the form of extended-Kalman filter, and in (Kumar and Das, 2017; Dezza et al., 2012) in the form of model reference adaptive observers (MRAO).

Due to the several merits of Backstepping estimation and observation mechanism, it is used for the control and estimation of machine variables (Morawiec, 2015; Trabelsi et al., 2012). It is also used for estimating the system's uncertainties as presented in (Krstić et al., 1995). The backstepping principle is also utilized to estimate the speed of induction motor as in (Morawiec, 2015; Stojić et al., 2015; Sun et al., 2016; Holtz, 2006). It is also adopted to observe the speed of the PMSM as presented in (Ni et al., 2017; Zhang et al., 2016). However, using the backstepping observation technique with the DFIG is still limited and the principle is only adopted as a control system and not as an observer (Xiong and Sun, 2016; Wang et al., 2017; Li et al., 2018). For this reason, the current paper concerns with exploiting the backstepping theory which proved its ability in handling high non-linearities and keeping minimum estimation error as well. The proposed backstepping estimator is designed in details and tested for a variable speed range of wind speed. The obtained results as it will be presented later confirm the validity of the designed observer in achieving an accurate estimation of the state variables.

Then, the contributions of the current study can be itemized by:

- The study presents a PPFC approach for a wind driven DFIG with the advantages of reduced ripples and reduced switching frequency.
- A comprehensive comparison between the proposed PPFC and the well-known PTC scheme is accomplished, showing the ability of the proposed PPFC in achieving better dynamics.
- The design and mathematical derivation of the proposed PPFC are carried out in simple and organized steps.
- The study proposed a robust observer for estimating the rotor's speed and position and other state variables depending on the backstepping theory.
- The study tested effectively the observer's dynamic for a variable wind speed operation to approve its feasibility.
- The proposed PPFC and the designed observer can be modified to be used for other machine types after considering the dynamics of each type.

The paper is organized as follows: In the first section, the equivalent model of DFIG and its wind turbine driving system considering the MPPT operation are explained in detail. In Section 2, the proposed PPFC is described and analyzed. In Section 3, the proposed speed/position estimator is designed and described. In Section 4, the complete control system is constructed and described. In Section 5, the test results for the two control mechanisms (PPT and proposed PPFC) are carried out and analyzed. In Section 6, the conclusions of the work are introduced.

2. Wind energy conversion system

2.1. Modeling of wind turbine and its MPPT mechanism

The wind turbine based energy system is illustrated in Fig. 1. This configuration represents the aerodynamic model of the turbine, in which the DFIG speed is represented by ω_g, meanwhile the turbine speed is given the symbol ω_t. It can be noticed that the turbine speed can managed by two ways; by regulating the blades pitch angle β or via controlling the torque (T_g) of the DFIG. The wind velocity V_w is treated as an external disturbance on the system. To evaluate the turbine speed (ω_t), a specified ratio entitled tip speed ratio (TSR) is used. The TSR refers to the ratio between the entering linear-speed to the blades and the wind velocity (Karakasis et al., 2019). Then the TSR can be expressed by,

$$\lambda = \frac{r\omega_t}{V_w} \tag{1}$$

where r is the radius of the blade.

In order to calculate the developed torque on the turbine shaft, the power coefficient C_P must be firstly evaluated as a function of λ and β (Taibi et al., 2014) as follows:

$$C_P = [0.5 - 0.00167\,(\beta - 2)]\sin\left[\frac{\pi\,(\lambda + 0.1)}{10 - 0.3\,(\beta - 2)}\right] - 0.00184\,(\lambda - 3)\,(\beta - 2) \tag{2}$$

The wind power can be also calculated by

$$P_w = \frac{1}{2}\rho A V_w^3 \tag{3}$$

where ρ is the air density, and A is the swept area.

The relationship between the wind power (P_w) and turbine power is given by

$$P_t = C_P P_w = C_P.\frac{1}{2}\rho A V_w^3 \tag{4}$$

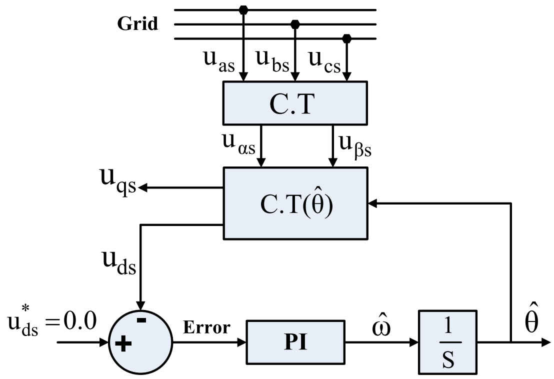

Fig. 4. PLL system configuration.

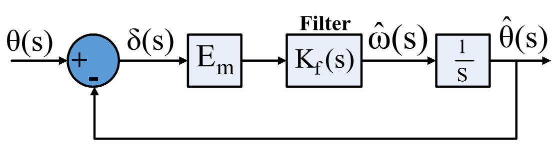

Fig. 5. PLL system after linearization.

Then, from (1), (2), (3) and (4), the turbine torque can be calculated by

$$T_t = \frac{P_t}{\omega_t} = \frac{C_P.\frac{1}{2}\rho A V_w^3}{\omega_t} \tag{5}$$

Two make a balance between the slow shaft (turbine shaft) and the fast shaft (generator's shaft), a gearbox ratio G must be used, so that the speed (ω_g) and torque (T_g) of the generator can be then given by

$$\omega_g = G\omega_t \tag{6}$$

$$T_g = \frac{T_t}{G} \tag{7}$$

Meanwhile, the mechanical shaft itself can be represented using a two-mass model (Gaamouche et al., 2020) as follows:

$$T_t - GT_g - FG\omega_t = \left(\frac{J_t}{G} + GJ_g\right)\frac{d\omega_t}{dt} \tag{8}$$

where F is the friction constant, and J_g, J_t are the inertia of the generator and turbine, correspondingly.

For the maximum power extraction purpose, the turbine must be operated at an optimal value of TSR (λ_{opt}), using which the power coefficient exhibits its maximum value $C_{P,max}$, and this approves (2) assuming that the turbine is with fixed pitch and thus the blade angle β becomes zero.

From these assumptions, the reference turbine speed can be calculated by

$$\omega_t^* = \frac{\lambda_{opt} V_w}{r} \tag{9}$$

Consequently, the reference generator's speed is given by

$$\omega_g^* = G\omega_t^* \tag{10}$$

The overall layout of the conversion system which summarizes the previous calculations is shown in Fig. 1.

2.2. Modeling of DFIG

The design of the proposed PPFC depends on the analysis of the relationship between the generator's torque and the power angle (δ) which is the same angle between the stator and rotor flux vectors. To start the analysis, a mathematical model of DFIG is firstly described. The model presents the equivalent circuit of DFIG in a synchronous rotating frame which has the same angular frequency of stator flux ($\omega_{\overline{\psi}_s}$). Fig. 2 shows the circuit model of DFIG in which all variables are expressed in the stator flux "sf" frame in which the flux vector $\overline{\psi}_s$ is totally allocated in the d-axis of rotating frame, and rotates with a speed of $\omega_{\overline{\psi}_s}$. Meanwhile, the stator voltage vector $\overline{u}_s$ is aligned to the q-axis of the rotating frame as shown in Fig. 2 which illustrates the vectors displacements in different co-ordinations.

Then, from Fig. 1, the dynamics of the DFIG can be discretely represented at instant KT_s, where T_s is the sampling time as follows;

$$\frac{d\psi^{sf}_{ds,k}}{dt} = u^{sf}_{ds,k} - R_s i^{sf}_{ds,k} + \omega_{\overline{\psi}_{s,k}}\psi^{sf}_{qs,k} \tag{11}$$

$$\frac{d\psi^{sf}_{qs,k}}{dt} = u^{sf}_{qs,k} - R_s i^{sf}_{qs,k} - \omega_{\overline{\psi}_{s,k}}\psi^{sf}_{ds,k} \tag{12}$$

$$\frac{di^{sf}_{dr,k}}{dt} = \left(\frac{L_m^2+\sigma L_s L_r}{\sigma L_s L_r^2}\right) * \left[u^{sf}_{dr,k} - R_r i^{sf}_{dr,k} + \frac{L_r}{L_m}\overbrace{\left(\omega_{\overline{\psi}_{s,k}} - \omega_{me,k}\right)}^{\omega_{slip,k}} \times \left(\psi^{sf}_{qs,k} - \sigma L_s i^{sf}_{qs,k}\right)\right] - \frac{L_m}{\sigma L_s L_r} * \left[u^{sf}_{ds,k} - R_s i^{sf}_{ds,k} + \omega_{\overline{\psi}_{s,k}}\psi^{sf}_{qs,k}\right] \tag{13}$$

$$\frac{di^{sf}_{qr,k}}{dt} = \left(\frac{L_m^2+\sigma L_s L_r}{\sigma L_s L_r^2}\right) * \left[u^{sf}_{qr,k} - R_r i^{sf}_{qr,k} - \frac{L_r}{L_m}\omega_{slip,k}\left(\psi^{sf}_{ds,k} - \sigma L_s i^{sf}_{ds,k}\right)\right] - \frac{L_m}{\sigma L_s L_r} * \left[u^{sf}_{qs,k} - R_s i^{sf}_{qs,k} - \omega_{\overline{\psi}_{s,k}}\psi^{sf}_{ds,k}\right] \tag{14}$$

$$\frac{d\omega_{me,k}}{dt} = \frac{p}{J}\left(T_{me,k} - T_{e,k}\right) \tag{15}$$

The generator's torque is calculated by

$$T_{e,k} = 1.5p\frac{L_m}{L_s}\left(\psi^{sf}_{ds,k} i^{sf}_{qr,k} - \psi^{sf}_{qs,k} i^{sf}_{dr,k}\right) \tag{16}$$

where R_s, R_r are the stator and rotor windings resistances, and L_s, L_r and L_m are the inductances of stator rotor and mutual coupling, respectively. The factor $\sigma = 1 - \frac{L_m^2}{L_s L_r}$ is used to express the leakage factor. The subscript $_s$ refers to the stator variables, while $_r$ refers to the rotor ones. The superscript ^{sf} refers to the stator flux frame. The mechanical (provided by the turbine) and generated torques are represented by T_{me} and T_e, respectively. While the synchronous and rotor speeds are expressed by $\omega_{\overline{\psi}_s}$ and ω_{me}. The generator pole pairs and its inertia are represented by p and J, respectively.

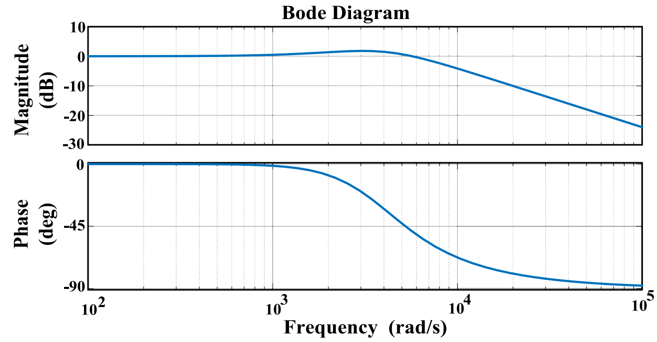

Fig. 6. Bode plot for closed loop transfer function of PLL system.

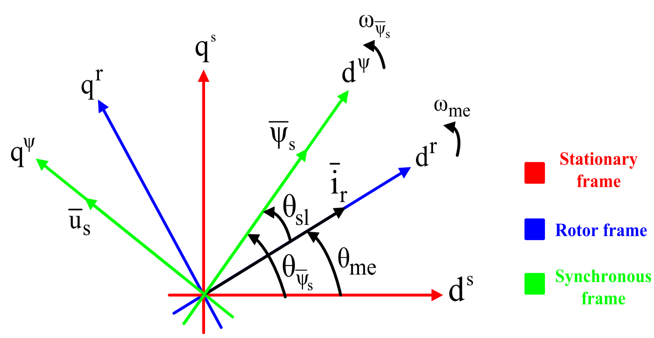

Fig. 7. Allocations of stator flux and rotor current vectors in space.

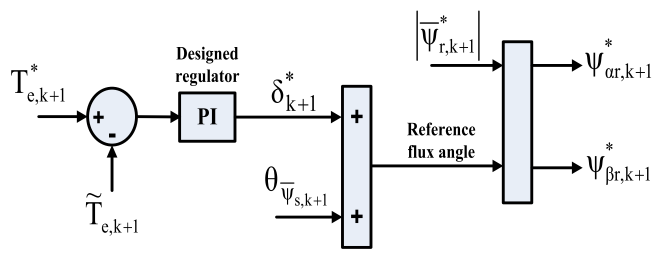

Fig. 8. Reference flux calculation.

2.3. Phase locked loop (PLL) system

The PLL is used to identify the angle $\hat{\theta}$ which is used for the co-ordinates transformation of stator voltage $\bar{u}_s$ so that it becomes totally oriented to the q-axis as illustrated in Fig. 3. The scheme of the PLL system is shown in Fig. 4.

As illustrated in Fig. 4, the PLL takes the grid voltages u_{abcs} as inputs and transforms it to d-q components. The alignment of stator voltage to the q-axis is performed via comparing the d-axis component with zero reference value. The resulted error is then fed to a PI adaptor to get the angular frequency ($\hat{\omega}$) of the voltage signal.

The grid voltages are calculated by:

$$u_{abcs} = U_m . \begin{pmatrix} \cos\theta \\ \cos\left(\theta - \frac{2\pi}{3}\right) \\ \cos\left(\theta + \frac{2\pi}{3}\right) \end{pmatrix} \tag{17}$$

where $u_{abcs} = [u_{as} \quad u_{bs} \quad u_{cs}]^T$. For steady state operation, the α-β voltage components can be evaluated by

$$u_{\alpha\beta} = (C.T) .u_{abcs} \tag{18}$$

where $u_{\alpha\beta} = \left[u_\alpha \quad u_\beta\right]^T$, and $C.T$ denotes to transformation matrix which can be expressed by

$$C.T = \frac{2}{3} . \begin{pmatrix} 1 & -\frac{1}{2} & -\frac{1}{2} \\ 0 & -\frac{\sqrt{3}}{2} & \frac{\sqrt{3}}{2} \end{pmatrix} \tag{19}$$

Using the estimated angle $\hat{\theta}$, the d-q voltages can be obtained by

$$u_{qde} = C.T\left(\hat{\theta}\right) .u_{\alpha\beta} \tag{20}$$

where $u_{qde} = \left[u_{qe} u_{de}\right]^T$, and $C.T\left(\hat{\theta}\right)$ is a matrix that can be defined as follows

$$C.T\left(\hat{\theta}\right) = \begin{pmatrix} \cos\hat{\theta} & -\sin\hat{\theta} \\ \sin\hat{\theta} & \cos\hat{\theta} \end{pmatrix} \tag{21}$$

The d-axis voltage can be calculated by

$$u_{ds} = E_m \sin\delta = e \tag{22}$$

where $E_m = -U_m$, and $\delta = \theta - \hat{\theta}$. The frequency of the voltage signal can be then calculated by

$$\widehat{\omega} = \frac{d\hat{\theta}}{dt} = K_f .e \tag{23}$$

where K_f is the filter's gain. In the case of that the angle difference δ is very small, then (22) can be rewritten by

$$e \cong E_m \delta \tag{24}$$

Thus, via the suitable choice of the filter's gain K_f, the phase θ and frequency ω of the grid voltage can be accurately tracked.

The model expressed in Fig. 4 is then linearized to derive the transfer function of the filter. The resultant model of the PLL after the linearization is illustrated in Fig. 5.

The illustrated closed loop system in Fig. 5 can be described using a transfer function form of

$$H_c\left(s\right) = \frac{\hat{\theta}(s)}{\theta(s)} = \frac{K_f(s)E_m}{s + K_f(s)E_m} \tag{25}$$

$$H_\delta\left(s\right) = \frac{\delta(s)}{\theta(s)} = \frac{s}{s + K_f(s)E_m} \tag{26}$$

where $\theta(s)$, $\hat{\theta}(s)$ and $\delta(s)$ are the Laplace transform of θ, $\hat{\theta}$ and δ, correspondingly.

To design the PI, the second order loop (SOL) method is utilized, in which the frequency response of the PI can be represented by

$$K_f\left(s\right) = K_p . \left(\frac{1 + s\tau}{s\tau}\right) \tag{27}$$

where K_p and τ refer to the PI constants. The transfer functions of the linearized system in Fig. 5 can be reformulated according to the general expression of the SOL method by

$$H_c\left(s\right) = \frac{2\xi\omega_n s + \omega_n^2}{s^2 + 2\xi\omega_n s + \omega_n^2} \tag{28}$$

$$H_\delta\left(s\right) = \frac{s^2}{s^2 + 2\xi\omega_n s + \omega_n^2} \tag{29}$$

where

$$\omega_n = \sqrt{\frac{K_p E_m}{\tau}}, \quad \text{and} \quad \xi = \frac{K_p E_m}{2\omega_n} = \frac{\sqrt{\tau K_p E_m}}{2} \tag{30}$$

where $\omega_{n=}314$ (rad/sec) is the system's frequency, and $\xi = 0.707$ is the damping coefficient. Then, the filter's gains are evaluated using (25), (27) and (28) for $U_m = \sqrt{2} * 380 = 537$ V, to be as $K_p = 12.85$, and $\tau = 0.000427$.

The bode plot of the transfer function for the designed closed loop system is shown in Fig. 6. From this layout, it is confirmed that the designed PI gains exhibit appropriate phase alignment which in turns reflects the validness of the designed PLL.

3. Predictive torque control (PTC)

The predictive torque control (PTC) of DFIG was considered in several previous studies (Mondal and Kastha, 2015; Mohammadi et al., 2014), in which the cost function of the controller was

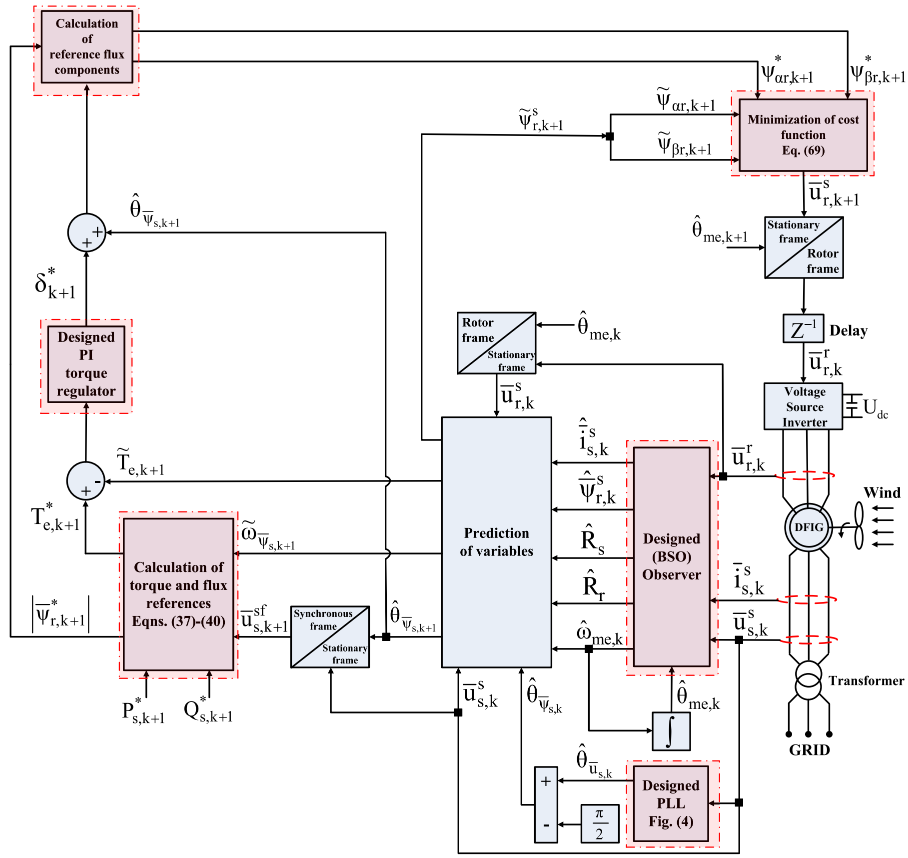

Fig. 9. Control system layout for the wind driven DFIG.

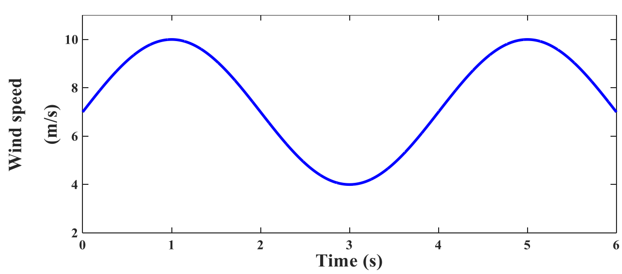

Fig. 10. Wind speed variation.

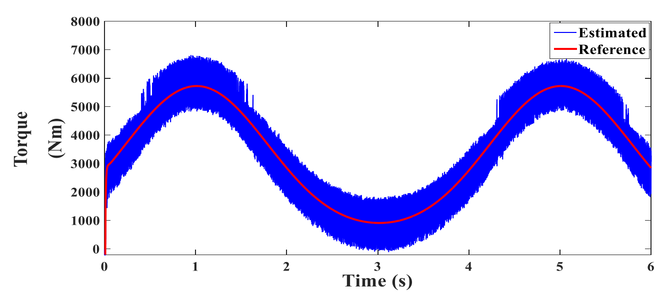

Fig. 12. Electromagnetic torque with PTC.

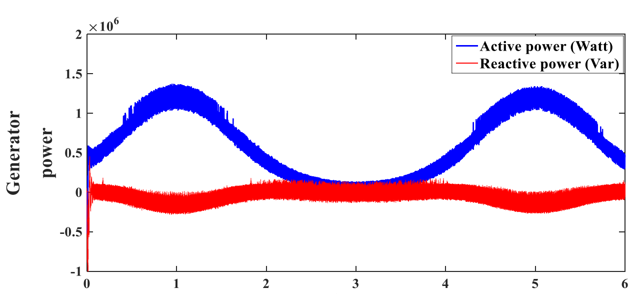

Fig. 11. Active and reactive power with PTC.

consisting of the torque and flux errors in addition to a weighting factor. The errors were calculated using the reference and predicted signals of torque and flux. The reference values are derived according to the active and reactive power requirements after considering a certain orientation control.

Under stator field orientation (SFO) as illustrated in Fig. 3, the stator flux is totally oriented to the d-axis of the rotating frame, meanwhile the stator voltage is oriented to the q-axis of the frame, and thus the following formulas are obtained

$$u^{sf}_{ds,k} = 0.0, \quad \text{and} \quad u^{sf}_{qs,k} = \left|\bar{u}_{s,k}\right| \tag{31}$$

$$\psi^{sf}_{ds,k} = \left|\bar{\psi}_{s,k}\right|, \quad \text{and} \quad \psi^{sf}_{qs,k} = 0.0 \tag{32}$$

Then, the active and reactive powers of the DFIG can be calculated under SFO by

$$P_{s,k} = 1.5 u^{sf}_{qs,k} i^{sf}_{qs,k} \tag{33}$$

$$Q_{s,k} = 1.5 u^{sf}_{qs,k} i^{sf}_{ds,k} \tag{34}$$

From (33) and (34), the reference values of d-q stator current components ($i^*_{ds,k}$, $i^*_{qs,k}$) are calculated in terms of the power

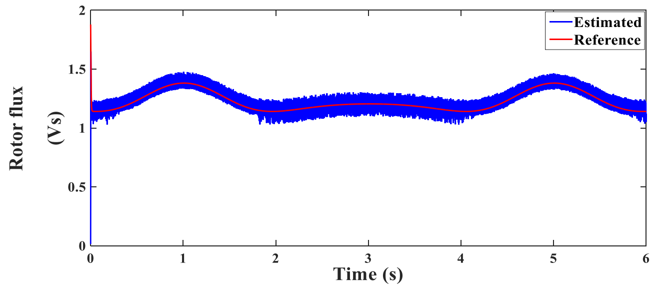

Fig. 13. Rotor flux with PTC.

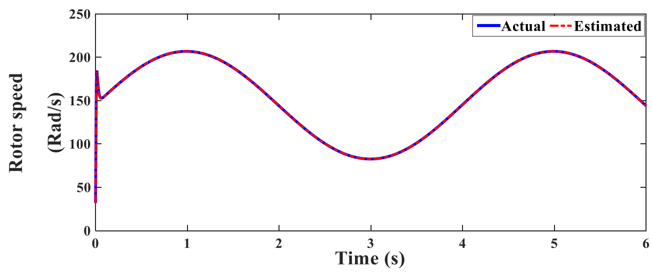

Fig. 14a. Generator shaft speed with PTC.

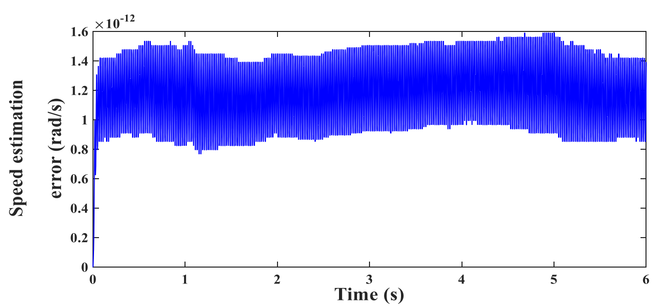

Fig. 14b. Speed estimation error with PTC.

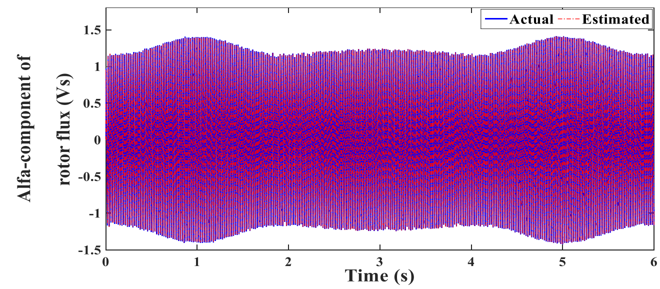

Fig. 15a. Actual and observed α-component of rotor flux with PTC.

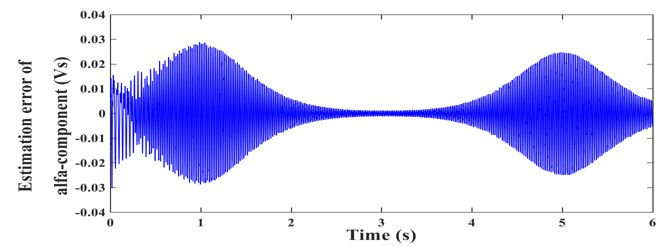

Fig. 15b. Observation error of rotor flux α-component with PTC.

references by

$$i^*_{ds,k} = \frac{Q^*_{s,k}}{1.5u^{sf}_{qs,k}}, \quad \text{and} \quad i^*_{qs,k} = \frac{P^*_{s,k}}{1.5u^{sf}_{qs,k}} \tag{35}$$

Via utilizing the current–flux association, the reference values of rotor current components ($i^*_{dr,k}$, $i^*_{qr,k}$) can be also computed as below

$$i^*_{dr,k} = \frac{u^{sf}_{qs,k}}{\mathrm{L_m}\omega_{\overline{\psi}_{s,k}}} - \frac{Q^*_{s,k}}{1.5\frac{\mathrm{L_m}}{\mathrm{L_s}}u^{sf}_{qs,k}}, \quad \text{and} \quad i^*_{qr,k} = \frac{-P^*_{s,k}}{1.5\frac{\mathrm{L_m}}{\mathrm{L_s}}u^{sf}_{qs,k}} \tag{36}$$

Then, from (35) and (36), the reference values of the torque and rotor flux to be used by the PTC can be calculated by

$$T^*_{e,k} = 1.5p\left(\frac{u^{sf}_{qs,k}i^*_{qs,k} - R_s\left(i^*_{qs,k}\right)^2}{\omega_{\overline{\psi}_{s,k}}}\right) \tag{37}$$

$$\left|\overline{\psi}^*_{r,k}\right| = \sqrt{\left(L_r i^*_{dr,k} + L_m i^*_{ds,k}\right)^2 + \left(L_r i^*_{qr,k} + L_m i^*_{qs,k}\right)^2} \tag{38}$$

On the other side, the predicted values of torque and flux at instant *(k+1)*T_s can be calculated using the derivatives in (11) to (14) as follows:

The predicted flux *d-q* terms are calculated by

$$\begin{aligned}\widetilde{\psi}^{sf}_{dr,k+1} &= \psi^{sf}_{dr,k} + \left(\frac{d\psi^{sf}_{dr,k}}{dt}\right)T_s, \quad \text{and}\\ \widetilde{\psi}^{sf}_{qr,k+1} &= \psi^{sf}_{qr,k} + \left(\frac{d\psi^{sf}_{qr,k}}{dt}\right)T_s\end{aligned} \tag{39}$$

where $\frac{d\psi^{sf}_{dr,k}}{dt}$ and $\frac{d\psi^{sf}_{qr,k}}{dt}$ can be obtained using (11)–(14) as follows

$$\begin{aligned}\frac{d\psi^{sf}_{dr,k}}{dt} &= \frac{L_m}{L_s}\frac{d\psi^{sf}_{ds,k}}{dt} + \sigma L_r\frac{di^{sf}_{dr,k}}{dt}, \text{ and}\\ \frac{d\psi^{sf}_{qr,k}}{dt} &= \frac{L_m}{L_s}\frac{d\psi^{sf}_{qs,k}}{dt} + \sigma L_r\frac{di^{sf}_{qr,k}}{dt}\end{aligned} \tag{40}$$

Then, the absolute value of predicted flux is given by

$$\left|\widetilde{\psi}^{sf}_{r,k+1}\right| = \sqrt{\left(\widetilde{\psi}^{sf}_{dr,k+1}\right)^2 + \left(\widetilde{\psi}^{sf}_{qr,k+1}\right)^2} \tag{41}$$

The predicted torque can be calculated by

$$\widetilde{T}_{e,k+1} = 1.5p\frac{L_m}{L_s}\left[\widetilde{\psi}^{sf}_{qs,k+1}\widetilde{i}^{sf}_{dr,k+1} - \widetilde{\psi}^{sf}_{ds,k+1}\widetilde{i}^{sf}_{qr,k+1}\right] \tag{42}$$

where the predicted values of stator flux components and rotor current components given in (42) can be calculated using the relations of (11)–(14).

Finally, via utilizing (37), (38), (41) and (42), all terms of the cost function used by the PTC are obtained and the function is then calculated by

$$\nabla^i = \left|T^*_{e,k+1} - \widetilde{T}_{e,k+1}\right|^i + W_f\left|\overline{\psi}^*_{r,k} - \widetilde{\psi}^{sf}_{r,k+1}\right|^i \tag{43}$$

where i is the index, and W_f is the balance weight between the rotor flux and torque errors.

4. Proposed predictive polar flux control (PPFC)

The operation of the proposed PPFC is depended on regulating the angle between the stator and rotor flux vectors. This angle

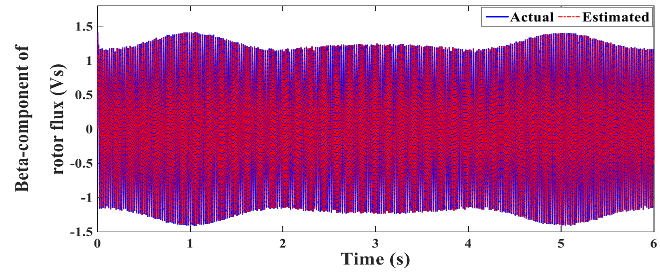

Fig. 16a. Actual and observed β-component of rotor flux with PTC.

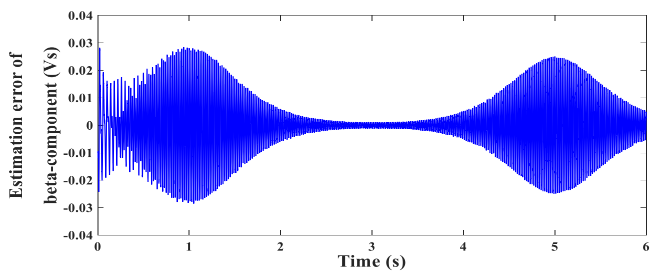

Fig. 16b. Observation error of rotor flux β –component with PTC.

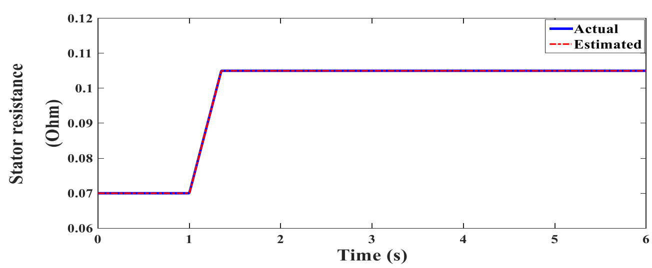

Fig. 17a. Real and observed stator resistance R_s with PTC.

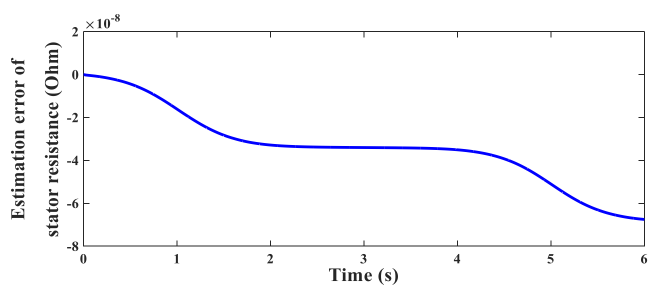

Fig. 17b. Observation error of R_s with PTC.

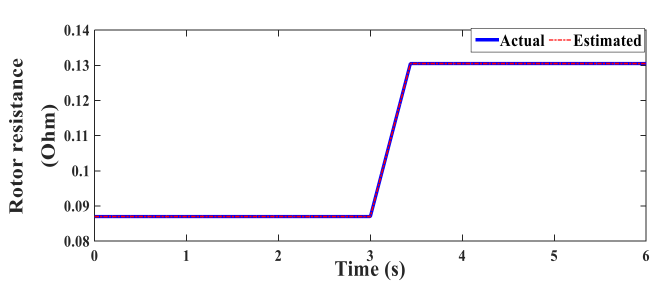

Fig. 18a. Real and observed rotor resistance R_r with PTC.

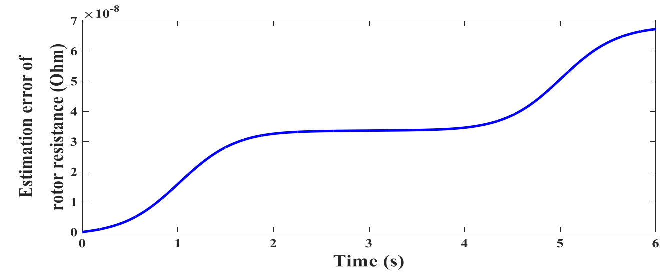

Fig. 18b. Observation error of R_r with PTC.

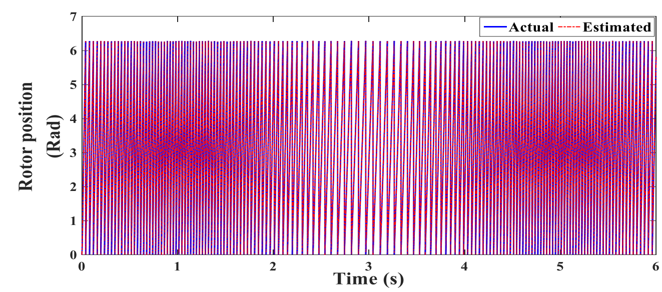

Fig. 19a. Real and observed rotor position θ_{me} with PTC.

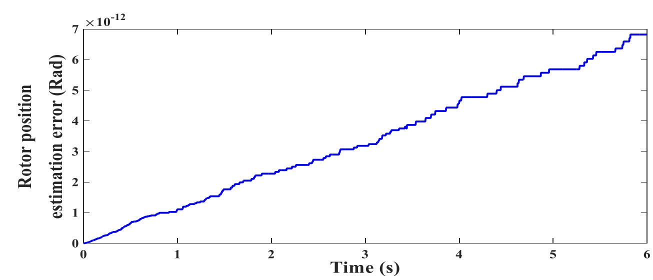

Fig. 19b. Rotor position estimation error with PTC.

is also representing the power angle (δ) of the DFIG as illustrated in Fig. 3. The regulation is completed through analyzing the power angle response to the variation in the torque, and to accomplish this task, the mathematical expression of the torque using different forms is used.

The encounter torque of DFIG can be expressed in terms of the power angle and magnitudes of the fluxes at instant *(k+1)*T_s by

$$T_{e,k+1} = 1.5p\frac{L_m}{\sigma L_s L_r}\left|\overline{\psi}_{s,k+1}\right|\left|\overline{\psi}_{r,k+1}\right|\sin\delta_{k+1} \tag{44}$$

The torque can be also obtained in terms of the angle between the stator flux vector $\overline{\psi}_{s,k+1}$ and rotor current vector $\overline{i}_{r,k+1}$. Considering the stator field orientation (SFO), the stator flux is completely oriented to the *d*-axis of the rotating frame; meanwhile the rotor current vector is aligned to the *d*-axis of the rotor frame as shown in Fig. 7. This means that the torque is proportional to the angle between the two vectors and which represents the slip angle $\theta_{sl,k+1}$, so the torque can be expressed by

$$T_{e,k+1} = 1.5p\frac{L_m}{L_s}\left|\overline{\psi}_{s,k+1}\right|\left|\overline{i}_{r,k+1}\right|\sin\theta_{sl,k+1} \tag{45}$$

Via comparing (44) and (45), a relation between the power angle δ_{k+1} and slip angle $\theta_{sl,k+1}$ is obtained as follows

$$\sin\delta_{k+1} = \left[1 - \frac{L_m}{L_s}\frac{\left|\overline{\psi}_{s,k+1}\right|}{\left|\overline{\psi}_{r,k+1}\right|}\right]\sin\theta_{sl,k+1} \tag{46}$$

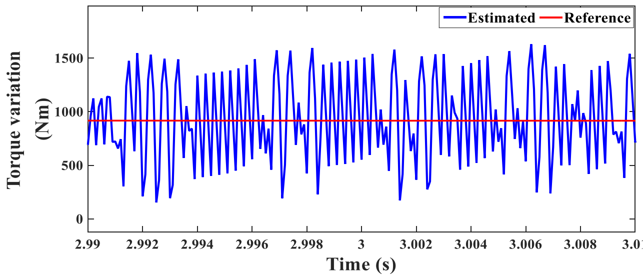

Fig. 20. Torque variation with PTC.

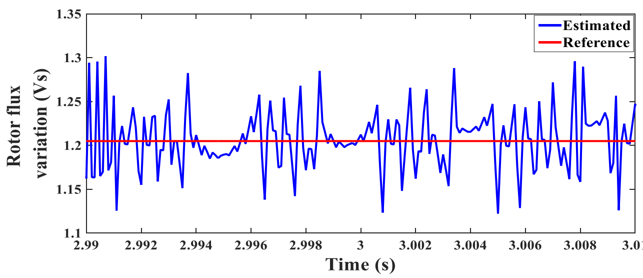

Fig. 21. Rotor flux variation with PTC.

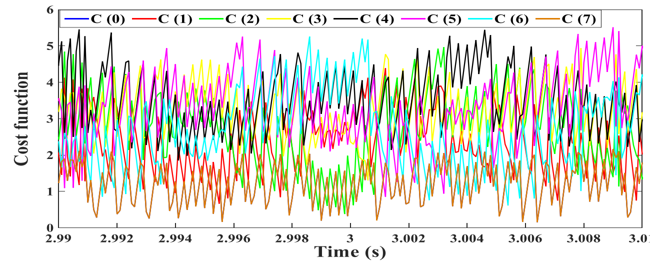

Fig. 22. Cost function values with PTC.

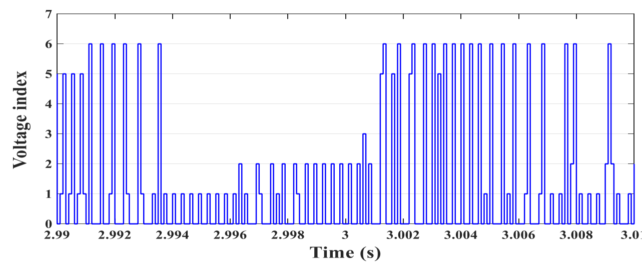

Fig. 23. Index variation with PTC.

Under steady state conditions, the amplitude of stator flux $|\overline{\psi}_s|$ is fixed and can be calculated by $|\overline{\psi}_s| = \frac{\overline{u}_s=380}{\omega_{\overline{\psi}_s}\cong 314} \cong 1.21$ Vs. Meanwhile, the rotor flux modulus is supposed to track its reference value which is calculated according to the active and reactive power requirements as expressed in (38), and then the rotor flux amplitude will be equal to $|\overline{\psi}_r| = |\overline{\psi}^*_r| = 1.223$ Vs.

Now, by substituting the flux values in (46), it results

$$\sin\delta_{k+1} = \left[1 - 0.989\frac{L_m}{L_s}\right]\sin\theta_{sl,k+1} \tag{47}$$

By taking the trigonometric inverse of (47), and differentiating the result, it gives

$$\frac{d\delta_{k+1}}{dt} = \left[1 - 0.989\frac{L_m}{L_s}\right]\omega_{sl,k+1} \tag{48}$$

The Eq. (48) represents the relation between the power angle variation and the angular slip frequency $\omega_{sl,k+1}$.

To express (48) in an operational form, the Laplace transform is taken which results in

$$\omega_{sl,k+1}(S) = \frac{S\delta_{k+1(S)}}{\left[1 - 0.989\frac{L_m}{L_s}\right]} \tag{49}$$

After getting the relation between the power angle and slip frequency as in (49), a relationship between the torque variation and slip frequency must be derived to help in getting the final relationship between the torque variation and power angle dynamic, and this is performed as follows:

The rotor voltage balance equation in rotor frame $^{(r)}$ can be described by

$$\overline{u}^r_{r,k+1} = R_r\overline{i}^r_{r,k+1} + \frac{d\overline{\psi}^r_{r,k+1}}{dt} \tag{50}$$

Moreover, the current–flux relationship can be represented by

$$\overline{\psi}^r_{r,k+1} = \frac{L_m}{L_s}\overline{\psi}^r_{s,k+1} + \sigma L_r\overline{i}^r_{r,k+1} \tag{51}$$

By substituting from (51) into (50), this results in

$$\frac{L_m}{L_s}\frac{d\overline{\psi}^r_{s,k+1}}{dt} = \overline{u}^r_{r,k+1} - R_r\overline{i}^r_{r,k+1} - \sigma L_r\frac{d\overline{i}^r_{r,k+1}}{dt} \tag{52}$$

The stator flux in the synchronous frame $^{(sf)}$ is rotating with a speed of $\omega_{\overline{\psi}_s}$ and can be defined in polar form by

$$\overline{\psi}^{sf}_{s,k+1} = \left|\overline{\psi}^*_{s,k+1}\right| . e^{j\omega_{\overline{\psi}_s}t} \tag{53}$$

The flux vector in (53) can be also defined in rotor frame $^{(r)}$ by

$$\overline{\psi}^r_{s,k+1} = \left|\overline{\psi}^*_{s,k+1}\right| . e^{j\left(\omega_{\overline{\psi}_s}-\omega_{me}\right)t} = \left|\overline{\psi}^*_{s,k+1}\right| . e^{j\omega_{sl,k+1}t} \tag{54}$$

Then, by substituting from (54) into (52), it gives

$$j\omega_{sl,k+1}\frac{L_m}{L_s}\overline{\psi}^r_{s,k+1} = \overline{u}^r_{r,k+1} - R_r\overline{i}^r_{r,k+1} - \sigma L_r\frac{d\overline{i}^r_{r,k+1}}{dt} \tag{55}$$

From (55), the rotor current vector expressed in operational form is given by

$$\overline{i}^r_{r,k+1}(S) = \frac{\overline{u}^r_{r,k+1} - j\omega_{sl,k+1}\frac{L_m}{L_s}\overline{\psi}^r_{s,k+1}(S)}{R_r + \sigma L_r S} \tag{56}$$

The encounter torque can be calculated using the following expression

$$T_{e,k+1} = 1.5p\frac{L_m}{L_s}I_m\left(\overline{\psi}^r_{s,k+1}.\check{\overline{i}}^r_{r,k+1}\right) \tag{57}$$

where I_m refers to the imaginary part, and $\check{}$ pertains to the conjugate operator.

Then, by substituting from (56) into (57), the relationship between the torque $T_{e,k+1}$ and angular slip $\omega_{sl,k+1}$ is obtained as follows

$$T_{e,k+1}(S) = \frac{1.5p\frac{L_m^2}{R_r L_s^2}\left|\overline{\psi}^r_{s,k+1}\right|^2}{1 + \frac{\sigma L_r}{R_r}S}\omega_{sl,k+1}(S) \tag{58}$$

The flux magnitude $\left|\overline{\psi}^r_{s,k+1}\right|$ in (58) has a fixed value in any reference frame equals to $\frac{\overline{u}_s}{\omega_{\overline{\psi}_s}} \cong 1.21$ Vs.

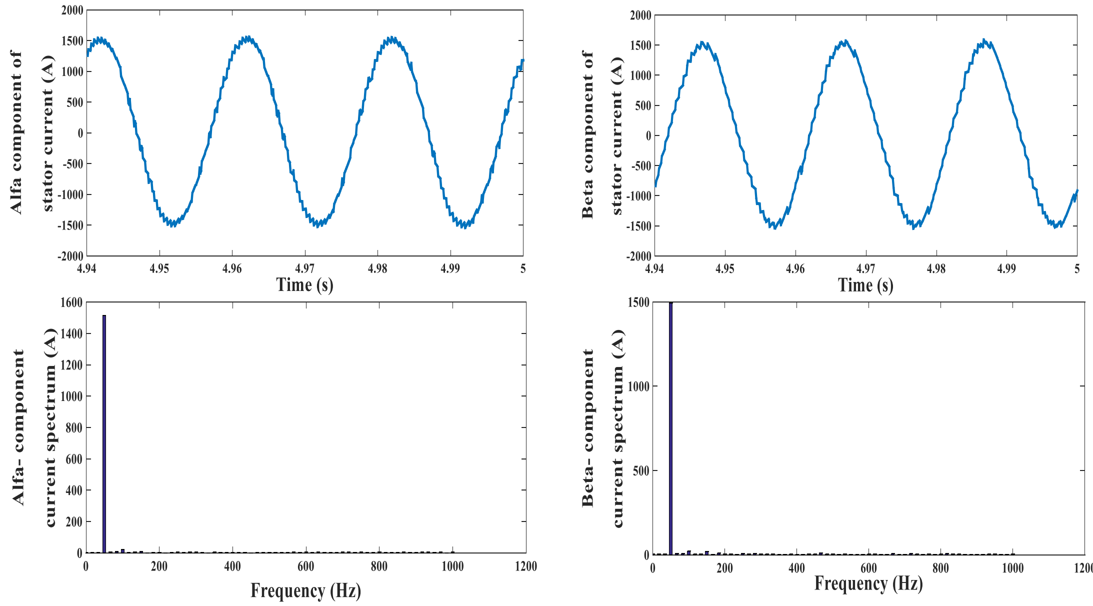

Fig. 24. Spectrums of α–β stator current components.

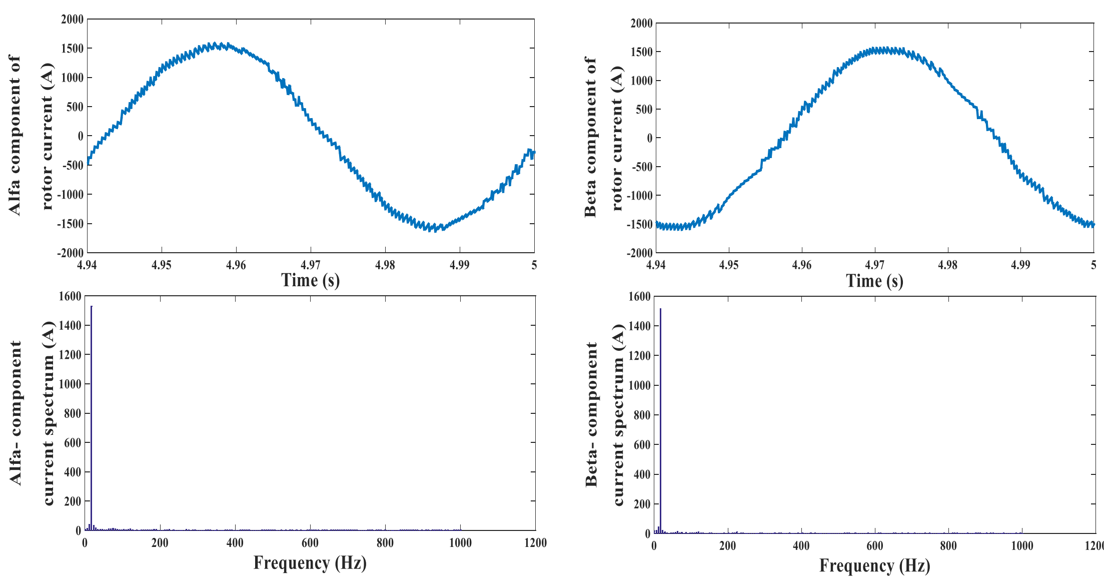

Fig. 25. Spectrums of α–β rotor current components.

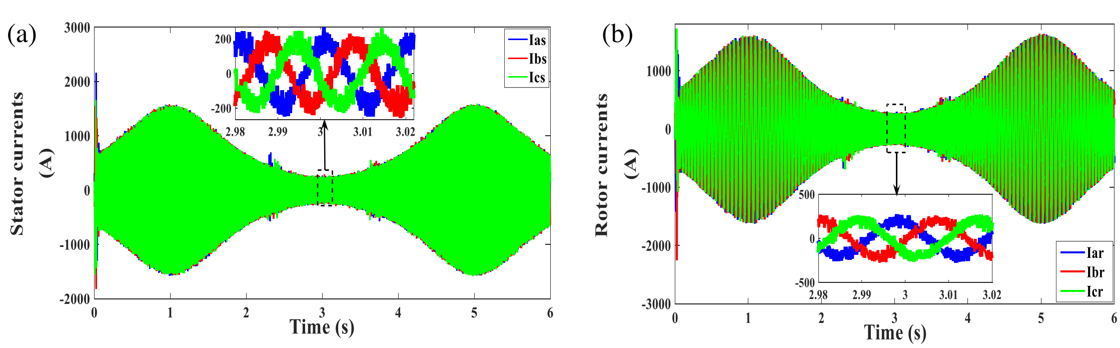

Fig. 26. (a) Stator currents, (b) Rotor currents.

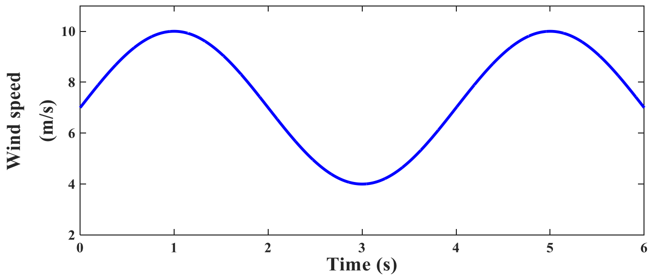

Fig. 27. Wind speed variation.

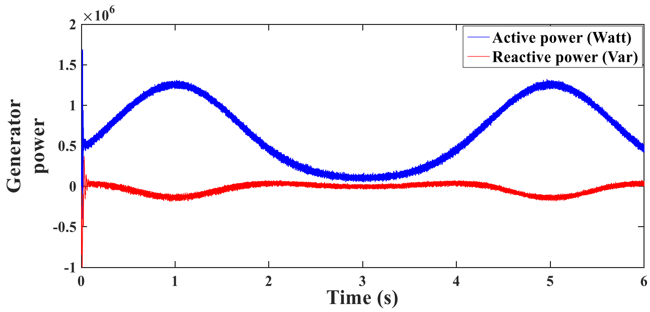

Fig. 28. Active and reactive power with PPFC.

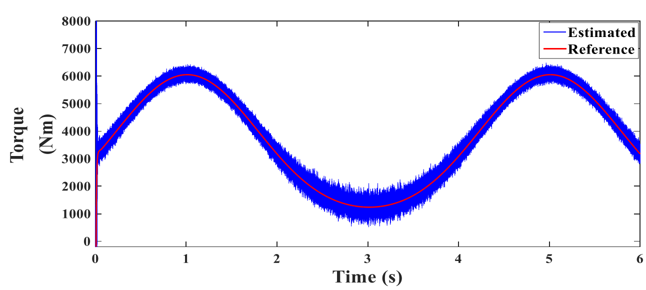

Fig. 29. Electromagnetic torque with PPFC.

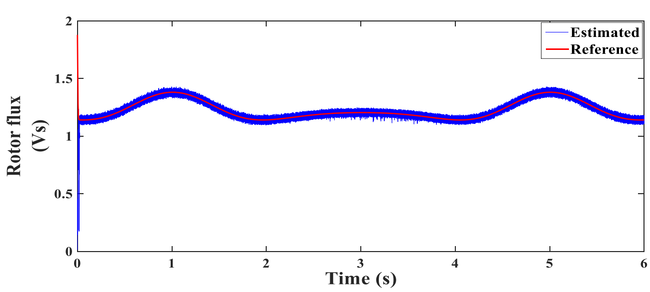

Fig. 30. Rotor flux with PPFC.

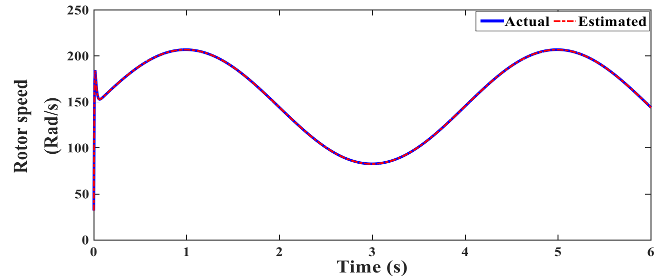

Fig. 31a. Generator shaft speed with PPFC.

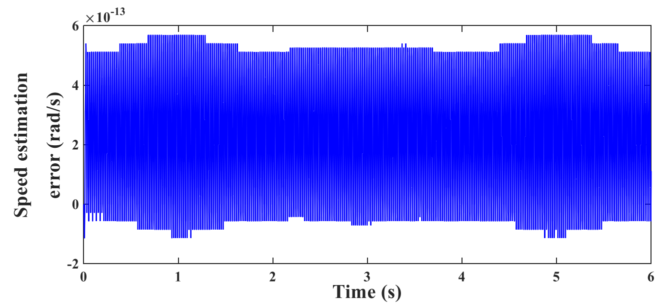

Fig. 31b. Speed estimation error with PPFC.

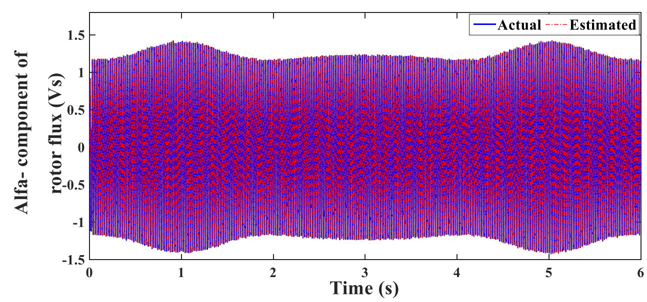

Fig. 32a. Actual and observed α-component of rotor flux with PPFC.

To simplify (58), lets $K = 1.5p\frac{L_m^2}{R_r L_s^2}\left|\overline{\psi}^r_{s,k+1}\right|^2$, and $T = \frac{\sigma L_r}{R_r}$. Then, by substituting from (49) into (58), the required torque–power angle relationship can be obtained as follows

$$T_{e,k+1}(S) = \frac{K}{1+TS}\frac{S\delta_{k+1(S)}}{\gamma} \tag{59}$$

where $\gamma = \left[1 - 0.989\frac{L_m}{L_s}\right]$.

Now, (59) can be utilized to design and determine the gains of the PI power angle regulator which is responsible for generating the reference power angle δ^*_{k+1} that will be used to calculate the reference components of rotor flux ($\psi^*_{\alpha r,k+1}$ and $\psi^*_{\beta r,k+1}$), which in turns are used by the cost function of the controller.

The operation of the PI regulator can be described by

$$\delta^*_{k+1}(S) = \left(K_p + \frac{K_i}{S}\right) * \left(T^*_{e,k+1}(S) - T_{e,k+1}(S)\right) \tag{60}$$

From (60), and by substituting in (59), it results

$$\frac{(1+TS)\,\gamma}{KS} T_{e,k+1}(S) = \left(K_p + \frac{K_i}{S}\right) * \left(T^*_{e,k+1}(S) - T_{e,k+1}(S)\right) \tag{61}$$

By dividing both sides by $T^*_{e,k+1}(S)$, and after arrangement, the transfer function which manages the operation of the PI regulator is expressed by

$$\frac{T_{e,k+1}(S)}{T^*_{e,k+1}(S)} = \frac{KK_pS^2 + KK_iS}{\left(KK_p + T\gamma\right)S^2 + (\gamma + KK_i)S} \tag{62}$$

To have a stable response, the roots of the denominator of (62) must be negative, which results in

$$\left(KK_p + T\gamma\right)S^2 + (\gamma + KK_i)S = 0.0 \tag{63}$$

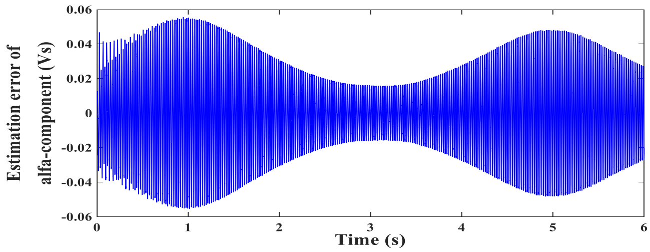

Fig. 32b. Observation error of rotor flux α-component with PPFC.

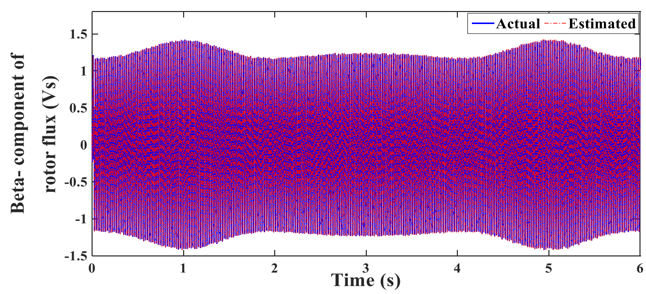

Fig. 33a. Actual and observed β-component of rotor flux with PPFC.

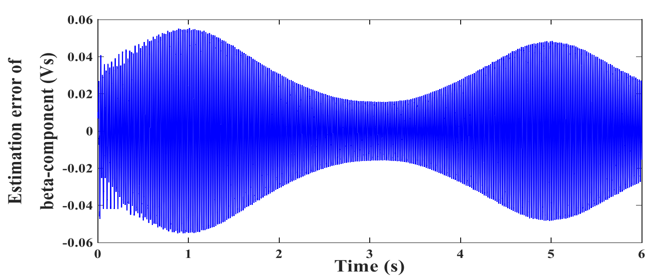

Fig. 33b. Observation error of rotor flux β –component with PPFC.

To derive the K_p and K_i values in (63). This second order equation must be compared with the polynomial equation of a second order system has a natural frequency of ω_n and damping coefficient of ζ and expressed mathematically by

$$S^2 + 2\zeta\ \omega_n S + \omega_n^2 = 0.0 \tag{64}$$

Thus, by comparing (63) and (64), the PI gains are calculated by

$$K_p = \frac{1 - T\gamma}{K}, \quad \text{and} \quad K_i = \frac{2\zeta\ \omega_n - \gamma}{K} \tag{65}$$

After obtaining the regulator's gain, and from Fig. 3, the developed reference power angle δ^*_{k+1} will be summed to the synchronous angle $\theta_{\overline{\psi}_{s,k+1}}$ to get finally the angle of the rotor flux vector. After that, by using the calculated angle and the reference rotor flux obtained by (38), the reference flux components ($\psi^*_{\alpha r,k+1}$ and $\psi^*_{\beta r,k+1}$) can be calculated by

$$\begin{aligned}\psi^*_{\alpha r,k+1} &= \left|\overline{\psi}^*_{r,k+1}\right| \cos\left(\delta^*_{k+1} + \theta_{\overline{\psi}_{s,k+1}}\right) \& \psi^*_{\beta r,k+1} \\ &= \left|\overline{\psi}^*_{r,k+1}\right| \sin\left(\delta^*_{k+1} + \theta_{\overline{\psi}_{s,k+1}}\right)\end{aligned} \tag{66}$$

The procedure of flux angle calculation is summarized in Fig. 8.

Now, all parts of the cost function to be used by the proposed PPFC are obtained, and the function can be formulated as follows

$$\forall^i = \left|\psi^*_{\alpha r,k+1} - \widetilde{\psi}_{\alpha r,k+1}\right|^i + \left|\psi^*_{\beta r,k+1} - \widetilde{\psi}_{\beta r,k+1}\right|^i \tag{67}$$

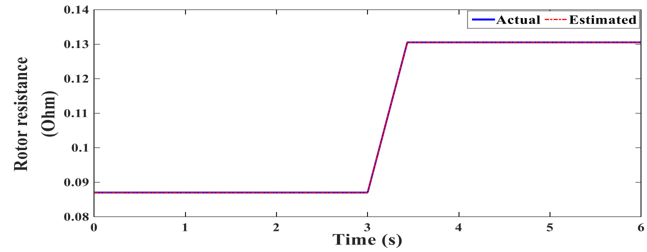

Fig. 34a. Real and observed stator resistance R_s with PPFC.

Comparing (67) with (43), it can be realized that the designed cost function is much simpler and has lower computation capacity which as a result reduces the switching losses and performed commutations as well. Moreover, there is no requirement for using a weighting quantity as both terms are of the same type (only flux variable). A comparison in terms of these two items is given in the results discussion section.

5. Designed observer

The observer is designed using the backstepping theory which is very suitable for handling the systems with high nonlinearities such as the DFIG's model. The operation of the designed observer stands on the error minimization between the observed and measured stator currents. The observer considers the measured currents and voltages as inputs and estimates the rotor speed, stator current, rotor flux and rotor and stator resistances too.

The observer can be mathematically modeled in (α–β) frame using the following expressions given at time KT_s

$$\begin{aligned}
\frac{d\hat{i}_{\alpha s,k}}{dt} &= \frac{1}{\sigma L_s}\Bigg[u_{\alpha s,k} - \frac{L_m}{L_r}u_{\alpha r,k} + \frac{L_m\hat{R}_r}{L_r^2}\hat{\psi}_{\alpha r,k} \\
&\quad + \frac{L_m}{L_r}\hat{\omega}_{me,k}\hat{\psi}_{\beta r,k} - \frac{\left(\hat{R}_s L_r^2 + \hat{R}_r L_m^2\right)}{L_r^2}\hat{\chi}_{\alpha,k}\Bigg] + \Gamma_{\alpha,k} \\
\frac{d\hat{i}_{\beta s,k}}{dt} &= \frac{1}{\sigma L_s}\Bigg[u_{\beta s,k} - \frac{L_m}{L_r}u_{\beta r,k} + \frac{L_m\hat{R}_r}{L_r^2}\hat{\psi}_{\beta r,k} \\
&\quad + \frac{L_m}{L_r}\hat{\omega}_{me,k}\hat{\psi}_{\alpha r,k} - \frac{\left(\hat{R}_s L_r^2 + \hat{R}_r L_m^2\right)}{L_r^2}\hat{\chi}_{\beta,k}\Bigg] + \Gamma_{\beta,k} \\
\frac{d\hat{\psi}_{\alpha r,k}}{dt} &= u_{\alpha r,k} - \frac{\hat{R}_r}{L_r}\hat{\psi}_{\alpha r,k} - \hat{\omega}_{me,k}\hat{\psi}_{\beta r,k} + \frac{L_m\hat{R}_r}{L_r}\hat{\chi}_{\alpha,k} \\
\frac{d\hat{\psi}_{\beta r,k}}{dt} &= u_{\beta r,k} - \frac{\hat{R}_r}{L_r}\hat{\psi}_{\beta r,k} + \hat{\omega}_{me,k}\hat{\psi}_{\alpha r,k} + \frac{L_m\hat{R}_r}{L_r}\hat{\chi}_{\beta,k}
\end{aligned} \tag{68}$$

where ^ refers to the observed variables, and $\hat{\chi}_{\alpha,k} = \hat{i}_{\alpha s,k}$ and $\hat{\chi}_{\beta,k} = \hat{i}_{\beta s,k}$. In addition, $\Gamma_{\alpha,k}$ and $\Gamma_{\beta,k}$ denote the vector components which are constructed using the backstepping methodology.

Using (68), the error model (annotated by ∼) can be described by the following differentials

$$\begin{aligned}
\frac{d\widetilde{i}_{\alpha s,k}}{dt} &= \frac{1}{\sigma L_s}\Bigg[\frac{L_m\widetilde{R}_r}{L_r^2}\psi_{\alpha r,k} + \frac{L_m\hat{R}_r}{L_r^2}\widetilde{\psi}_{\alpha r,k} + \frac{L_m}{L_r}\hat{\omega}_{me,k}\widetilde{\psi}_{\beta r,k} \\
&\quad + \frac{L_m}{L_r}\widetilde{\omega}_{me,k}\psi_{\beta r,k} - \frac{\left(\widetilde{R}_s L_r^2 + \widetilde{R}_r L_m^2\right)}{L_r^2}\widetilde{\chi}_{\alpha,k}\Bigg] + \Gamma_{\alpha,k} \\
\frac{d\widetilde{i}_{\beta s,k}}{dt} &= \frac{1}{\sigma L_s}\Bigg[\frac{L_m\widetilde{R}_r}{L_r^2}\psi_{\beta r,k} + \frac{L_m\hat{R}_r}{L_r^2}\widetilde{\psi}_{\beta r,k} - \frac{L_m}{L_r}\hat{\omega}_{me,k}\widetilde{\psi}_{\alpha r,k}
\end{aligned}$$

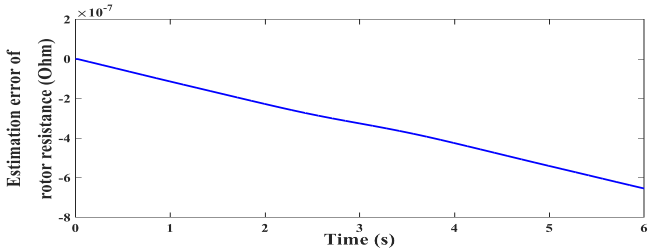

Fig. 34b. Observation error of R_s with PPFC.

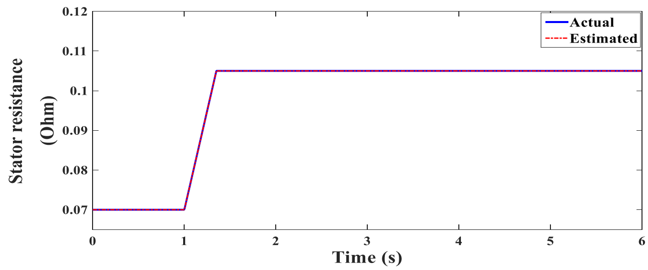

Fig. 35a. Real and observed rotor resistance R_r with PPFC.

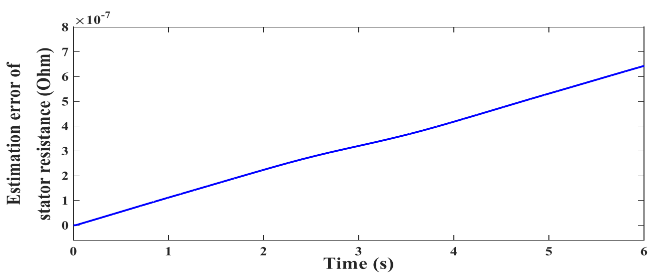

Fig. 35b. Observation error of R_r with PPFC.

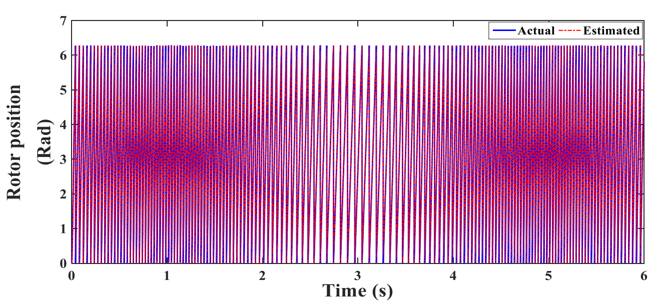

Fig. 36a. Real and observed rotor position θ_{me} with PPFC.

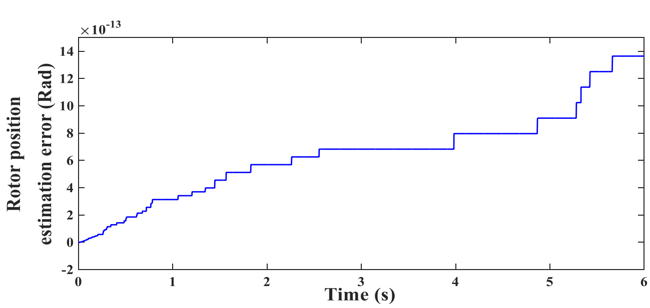

Fig. 36b. Rotor position estimation error with PPFC.

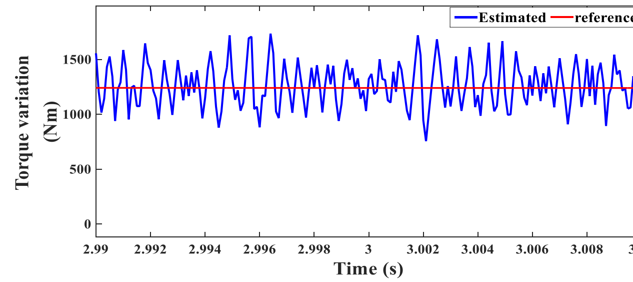

Fig. 37. Torque variation with PPFC.

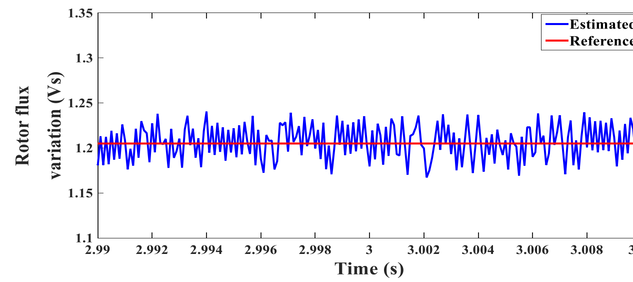

Fig. 38. Rotor flux variation with PPFC.

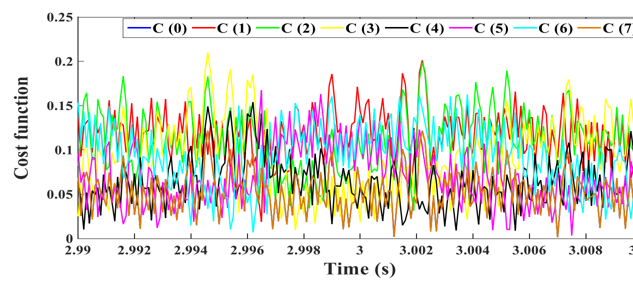

Fig. 39. Cost function values with PPFC.

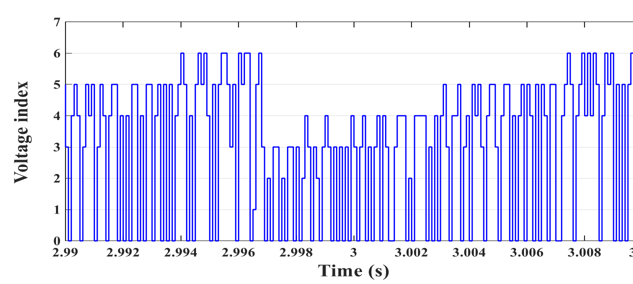

Fig. 40. Index variation with PPFC.

$$
\begin{aligned}
&\left.-\frac{L_m}{L_r}\widetilde{\omega}_{me,k}\psi_{\alpha r,k}-\frac{\left(\widetilde{R}_sL_r^2+\widetilde{R}_rL_m^2\right)}{L_r^2}\widetilde{\chi}_{\beta,k}\right]+\Gamma_{\beta,k}\\
&\frac{d\widetilde{\psi}_{\alpha r,k}}{dt}=u_{\alpha r,k}-\frac{\widetilde{R}_r}{L_r}\psi_{\alpha r,k}-\frac{\hat{R}_r}{L_r}\widetilde{\psi}_{\alpha r,k}-\hat{\omega}_{me,k}\widetilde{\psi}_{\beta r,k}\\
&-\widetilde{\omega}_{me,k}\psi_{\beta r,k}+\frac{L_m\hat{R}_r}{L_r}\widetilde{\chi}_{\alpha,k}\\
&\frac{d\widetilde{\psi}_{\beta r,k}}{dt}=u_{\beta r,k}-\frac{\widetilde{R}_r}{L_r}\psi_{\beta r,k}-\frac{\hat{R}_r}{L_r}\widetilde{\psi}_{\beta r,k}+\hat{\omega}_{me,k}\widetilde{\psi}_{\alpha r,k}\\
&+\widetilde{\omega}_{me,k}\psi_{\alpha r,k}+\frac{L_m\hat{R}_r}{L_r}\widetilde{\chi}_{\beta,k}
\end{aligned}
\tag{69}
$$

where $\widetilde{\chi}_{\alpha,k} = \widetilde{i}_{\alpha s,k} = \hat{i}_{\alpha s,k} - i_{\alpha s,k}$, $\widetilde{\chi}_{\beta,k} = \widetilde{i}_{\beta s,k} = \hat{i}_{\beta s,k} - i_{\beta s,k}$, $\widetilde{\psi}_{\alpha r,k} = \hat{\psi}_{\alpha r,k} - \psi_{\alpha r,k}$, $\widetilde{\psi}_{\beta r,k} = \hat{\psi}_{\beta r,k} - \psi_{\beta r,k}$, $\widetilde{\omega}_{me,k} = \hat{\omega}_{me,k} - \omega_{me,k}$, $\widetilde{R}_s = \hat{R}_s - R_s$ and $\widetilde{R}_r = \hat{R}_r - R_r$.

The observation procedure consists of two sequential stages. In the primary stage, a system is designed to integrate the observation errors ($\widetilde{\chi}_{\alpha,k}$, $\widetilde{\chi}_{\beta,k}$) using their virtual components ($\widetilde{i}_{\alpha s,k}$, $\widetilde{i}_{\beta s,k}$) in addition to their correspondent references ($f_{\alpha,k}$, $f_{\beta,k}$) which are used for the stabilization purpose. Consequently, the integral of the observation errors ($\tilde{e}_{\alpha,k}$, $\tilde{e}_{\beta,k}$) can be defined by

$$\frac{d\tilde{e}_{\alpha,k}}{dt} = \widetilde{i}_{\alpha s,k}, \quad \text{and} \quad \frac{d\tilde{e}_{\beta,k}}{dt} = \widetilde{i}_{\beta s,k} \tag{70}$$

By the subtraction and addition of $f_{\alpha,k}$ and $f_{\beta,k}$ from/to the expressions (69) and (70), the following relations are obtained

$$\frac{d\tilde{e}_{\alpha,k}}{dt} = Y_{\alpha,k} - S_1\tilde{e}_{\alpha,k}, \quad \text{and} \quad \frac{d\tilde{e}_{\beta,k}}{dt} = Y_{\beta,k} - S_1\tilde{e}_{\beta,k} \tag{71}$$

where $Y_{\alpha,k} = \widetilde{i}_{\alpha s,k} - f_{\alpha,k}$, $Y_{\beta,k} = \widetilde{i}_{\beta s,k} - f_{\beta,k}$. Meanwhile, $f_{\alpha,k} = -S_1\tilde{e}_{\alpha,k}$ and $f_{\beta,k} = -S_1\tilde{e}_{\beta,k}$. The constant S_1 is a positive factor.

The next step of the design is dedicated to the control of $Y_{\alpha,k}$ and $Y_{\beta,k}$ variables, which are derived from (71) by

$$Y_{\alpha,k} = \widetilde{i}_{\alpha s,k} + S_1\tilde{e}_{\alpha,k}, \quad \text{and} \quad Y_{\beta,k} = \widetilde{i}_{\beta s,k} + S_1\tilde{e}_{\beta,k} \tag{72}$$

Taking the derivative of (72), the following expressions are obtained

$$\frac{dY_{\alpha,k}}{dt} = \frac{1}{\sigma L_s}\left[\frac{L_m\widetilde{R}_r}{L_r^2}\psi_{\alpha r,k} + \frac{L_m\hat{R}_r}{L_r^2}\widetilde{\psi}_{\alpha r,k} + \frac{L_m}{L_r}\hat{\omega}_{me,k}\widetilde{\psi}_{\beta r,k} + \frac{L_m}{L_r}\widetilde{\omega}_{me,k}\psi_{\beta r,k} - \frac{\left(\widetilde{R}_s L_r^2 + \widetilde{R}_r L_m^2\right)}{L_r^2}\widetilde{\chi}_{\alpha,k}\right] + \Gamma_{\alpha,k} + S_1\widetilde{i}_{\alpha s,k} \tag{73}$$

$$\frac{dY_{\beta,k}}{dt} = \frac{1}{\sigma L_s}\left[\frac{L_m\widetilde{R}_r}{L_r^2}\psi_{\beta r,k} + \frac{L_m\hat{R}_r}{L_r^2}\widetilde{\psi}_{\beta r,k} - \frac{L_m}{L_r}\hat{\omega}_{me,k}\widetilde{\psi}_{\alpha r,k} - \frac{L_m}{L_r}\widetilde{\omega}_{me,k}\psi_{\alpha r,k} - \frac{\left(\widetilde{R}_s L_r^2 + \widetilde{R}_r L_m^2\right)}{L_r^2}\widetilde{\chi}_{\beta,k}\right] + \Gamma_{\beta,k} + S_1\widetilde{i}_{\beta s,k} \tag{74}$$

After that, the vectors $\Gamma_{\alpha,k}$ and $\Gamma_{\beta,k}$ can be designed using the following formulas

$$\begin{aligned}\Gamma_{\alpha,k} &= \frac{-1}{\sigma L_s}\left[\frac{L_m\hat{R}_r}{L_r^2}\widetilde{\psi}_{\alpha r,k} + \frac{L_m}{L_r}\hat{\omega}_{me,k}\widetilde{\psi}_{\beta r,k}\right] - S_1\widetilde{i}_{\alpha s,k} - S_2Y_{\alpha,k} - \tilde{e}_{\alpha,k}\\ \Gamma_{\beta,k} &= \frac{-1}{\sigma L_s}\left[\frac{L_m\hat{R}_r}{L_r^2}\widetilde{\psi}_{\beta r,k} - \frac{L_m}{L_r}\hat{\omega}_{me,k}\widetilde{\psi}_{\alpha r,k}\right] - S_1\widetilde{i}_{\beta s,k} - S_2Y_{\beta,k} - \tilde{e}_{\beta,k}\end{aligned} \tag{75}$$

In (75), the factor S_2 is also with a positive value.

Now by replacing from (75) into (73) and (74), the following is obtained

$$\frac{dY_{\alpha,k}}{dt} = \frac{1}{\sigma L_s}\left[\frac{L_m\widetilde{R}_r}{L_r^2}\psi_{\alpha r,k} + \frac{L_m}{L_r}\widetilde{\omega}_{me,k}\psi_{\beta r,k} - \frac{\left(\widetilde{R}_s L_r^2 + \widetilde{R}_r L_m^2\right)}{L_r^2}\widetilde{\chi}_{\alpha,k}\right] - S_2Y_{\alpha,k} - \tilde{e}_{\alpha,k} \tag{76}$$

$$\frac{dY_{\beta,k}}{dt} = \frac{1}{\sigma L_s}\left[\frac{L_m\widetilde{R}_r}{L_r^2}\psi_{\beta r,k} - \frac{L_m}{L_r}\widetilde{\omega}_{me,k}\psi_{\alpha r,k} - \frac{\left(\widetilde{R}_s L_r^2 + \widetilde{R}_r L_m^2\right)}{L_r^2}\widetilde{\chi}_{\beta,k}\right] - S_2Y_{\beta,k} - \tilde{e}_{\beta,k} \tag{77}$$

To check the stability of the designed observer, the following Lyapunov's function is used,

$$L = \frac{1}{2}\left(\tilde{e}_{\alpha,k}^2 + \tilde{e}_{\beta,k}^2 + Y_{\alpha,k}^2 + Y_{\beta,k}^2 + \widetilde{\psi}_{\alpha r,k}^2 + \widetilde{\psi}_{\beta r,k}^2 + \frac{1}{C_s}\widetilde{R}_s^2 + \frac{1}{C_r}\widetilde{R}_r^2 + \frac{1}{C_\omega}\widetilde{\omega}_{me,k}^2\right) \tag{78}$$

where C_s, C_r and C_ω are positive definite.

Taking the derivative of (78), and by utilizing (69), (71), (76) and (77), it gives

$$\begin{aligned}\frac{dL}{dt} &= -S_1\tilde{e}_{\alpha,k}^2 - S_1\tilde{e}_{\beta,k}^2 - S_2Y_{\alpha,k}^2 - S_2Y_{\beta,k}^2 - \frac{\hat{R}_r}{L_r}\widetilde{\psi}_{\alpha r,k}^2 - \frac{\hat{R}_r}{L_r}\widetilde{\psi}_{\beta r,k}^2\\ &+ \widetilde{R}_s\left[\frac{-1}{\sigma L_s}Y_{\alpha,k}\widetilde{\chi}_{\alpha,k} - \frac{1}{\sigma L_s}Y_{\beta,k}\widetilde{\chi}_{\beta,k} + \frac{1}{C_s}\frac{d\widetilde{R}_s}{dt}\right] + \widetilde{R}_r\left[\frac{L_m}{\sigma L_s L_r^2}Y_{\alpha,k}\psi_{\alpha r,k}\right.\\ &+ \frac{L_m}{\sigma L_s L_r^2}Y_{\beta,k}\psi_{\beta r,k} - \frac{L_m^2}{\sigma L_s L_r^2}Y_{\alpha,k}\widetilde{\chi}_{\alpha,k} - \frac{L_m^2}{\sigma L_s L_r^2}Y_{\beta,k}\widetilde{\chi}_{\beta,k} - \frac{\widetilde{\psi}_{\alpha r,k}\psi_{\alpha r,k}}{L_r} - \frac{\widetilde{\psi}_{\beta r,k}\psi_{\beta r,k}}{L_r} + \frac{L_m}{L_r}\widetilde{\chi}_{\alpha,k}\widetilde{\psi}_{\alpha r,k}\\ &\left. + \frac{L_m}{L_r}\widetilde{\chi}_{\beta,k}\widetilde{\psi}_{\beta r,k} + \frac{1}{C_r}\frac{d\widetilde{R}_r}{dt}\right] + \widetilde{\omega}_{me,k}\left[\frac{L_m}{\sigma L_s L_r}\widetilde{\psi}_{\beta r,k} - \frac{L_m}{\sigma L_s L_r}\widetilde{\psi}_{\alpha r,k} + \frac{1}{C_\omega}\frac{d\widetilde{\omega}_{me,k}}{dt}\right]\end{aligned} \tag{79}$$

A negative definite of L is a requirement to have a stable dynamic, and this can be obtained by considering the following conditions,

$$\widetilde{R}_s\left\{-\frac{1}{\sigma L_s}Y_{\alpha,k}\widetilde{\chi}_{\alpha,k} - \frac{1}{\sigma L_s}Y_{\beta,k}\widetilde{\chi}_{\beta,k} + \frac{1}{C_s}\frac{d\widetilde{R}_s}{dt}\right\} = 0.0 \tag{80}$$

$$\widetilde{R}_r\left[\frac{L_m}{\sigma L_s L_r^2}Y_{\alpha,k}\psi_{\alpha r,k} + \frac{L_m}{\sigma L_s L_r^2}Y_{\beta,k}\psi_{\beta r,k} - \frac{L_m^2}{\sigma L_s L_r^2}Y_{\alpha,k}\widetilde{\chi}_{\alpha,k} - \frac{L_m^2}{\sigma L_s L_r^2}Y_{\beta,k}\widetilde{\chi}_{\beta,k} - \frac{\widetilde{\psi}_{\alpha r,k}\psi_{\alpha r,k}}{L_r} - \frac{\widetilde{\psi}_{\beta r,k}\psi_{\beta r,k}}{L_r} + \frac{L_m}{L_r}\widetilde{\chi}_{\alpha,k}\widetilde{\psi}_{\alpha r,k} + \frac{L_m}{L_r}\widetilde{\chi}_{\beta,k}\widetilde{\psi}_{\beta r,k} + \frac{1}{C_r}\frac{d\widetilde{R}_r}{dt}\right] = 0.0 \tag{81}$$

$$\widetilde{\omega}_{me,k}\left[\frac{L_m}{\sigma L_s L_r}\widetilde{\psi}_{\beta r,k} - \frac{L_m}{\sigma L_s L_r}\widetilde{\psi}_{\alpha r,k} + \frac{1}{C_\omega}\frac{d\widetilde{\omega}_{me,k}}{dt}\right] \tag{82}$$

From (80), (81) and (82), the adaptation expressions through which the stator and rotor resistances and rotor speed can be estimated are written by

$$\frac{d\widetilde{R}_s}{dt} = \frac{C_s}{\sigma L_s}\left\{Y_{\alpha,k}\widetilde{\chi}_{\alpha,k} + Y_{\beta,k}\widetilde{\chi}_{\beta,k}\right\} \tag{83}$$

$$\frac{d\widetilde{R}_r}{dt} = C_r\left\{\frac{-L_m}{\sigma L_s L_r^2}Y_{\alpha,k}\psi_{\alpha r,k} - \frac{L_m}{\sigma L_s L_r^2}Y_{\beta,k}\psi_{\beta r,k} + \frac{L_m^2}{\sigma L_s L_r^2}Y_{\alpha,k}\widetilde{\chi}_{\alpha,k} + \frac{L_m^2}{\sigma L_s L_r^2}Y_{\beta,k}\widetilde{\chi}_{\beta,k} + \frac{\widetilde{\psi}_{\alpha r,k}\psi_{\alpha r,k}}{L_r} + \frac{\widetilde{\psi}_{\beta r,k}\psi_{\beta r,k}}{L_r} - \frac{L_m}{L_r}\widetilde{\chi}_{\alpha,k}\widetilde{\psi}_{\alpha r,k} - \frac{L_m}{L_r}\widetilde{\chi}_{\beta,k}\widetilde{\psi}_{\beta r,k}\right\} \tag{84}$$

$$\frac{d\widetilde{\omega}_{me}}{dt} = C_\omega\left\{\frac{L_m}{\sigma L_s L_r}\widetilde{\psi}_{\alpha r} - \frac{L_m}{\sigma L_s L_r}\widetilde{\psi}_{\beta r}\right\} \tag{85}$$

Now, the resistances and speed can be appropriately estimated and then used by the controller.

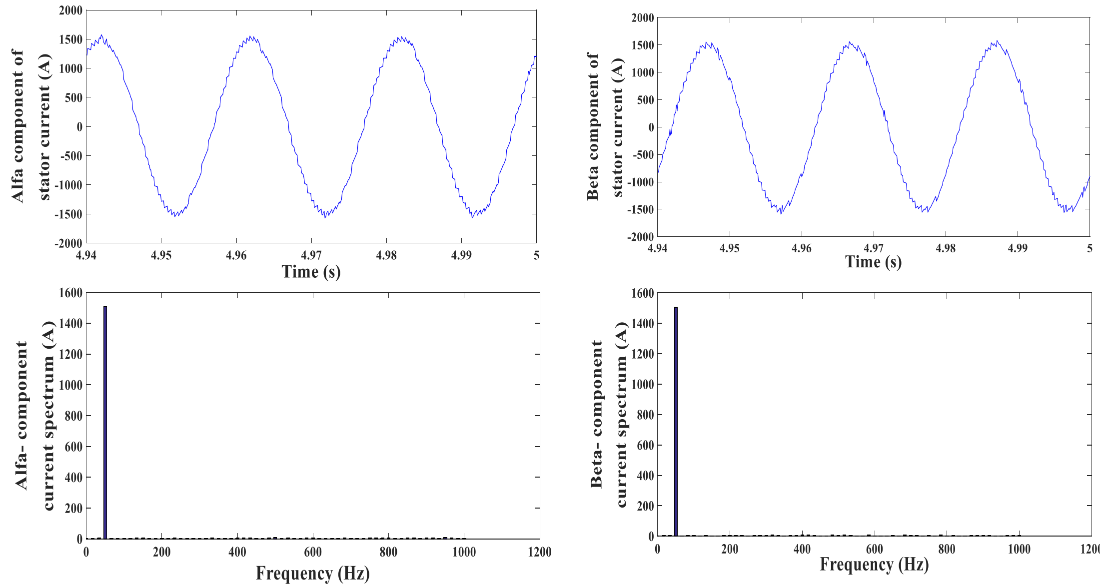

Fig. 41. Spectrums of α-β stator current components with PPFC.

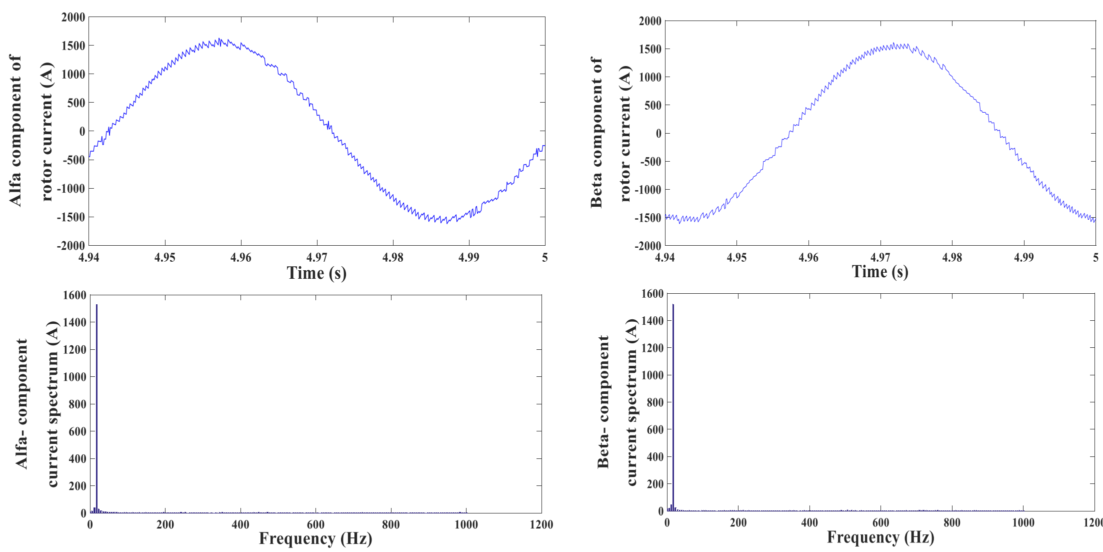

Fig. 42. Spectrums of α-β rotor current components with PPFC.

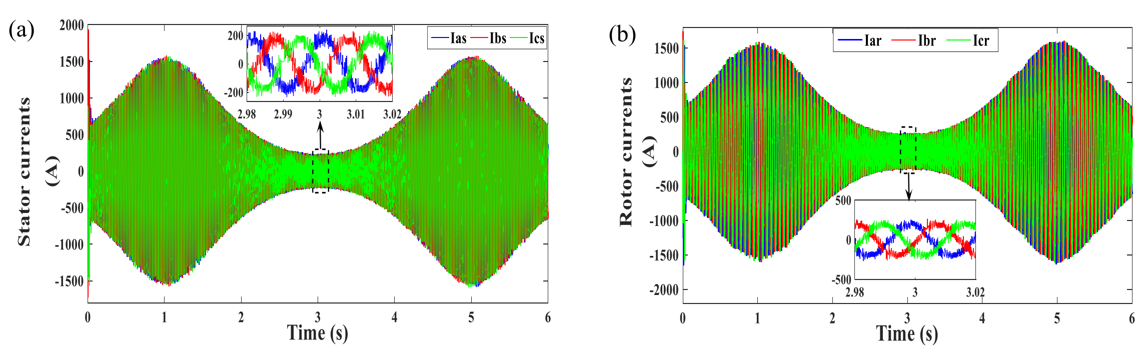

Fig. 43. (a) Stator currents, (b) Rotor currents.

6. Control system layout

After designing the observer, all system components are now available and can be connected together to construct the general structure of the proposed control system. As shown in Fig. 9, the system consists of a DFIG which is driven by a wind turbine system described earlier in Section 2.1. The control is performed through the rotor side, meanwhile the stator terminals of the generator are connected to the grid via a transformer. The designed PLL described in Section 2.3 is used to observe the voltage phase $\hat{\theta}_{\overline{u}_{s,k}}$ and consequently the stator flux phase angle $\hat{\theta}_{\overline{\psi}_{s,k}}$ can be obtained. The flux angle is the same angle of the rotating frame, and is used besides the estimated rotor angle $\hat{\theta}_{me,k}$ for the co-ordinates transformation purpose. The designed observer is used to observe the stator current $\hat{i}^{s}_{s,k}$, rotor flux $\hat{\psi}^{s}_{r,k}$, rotor speed $\hat{\omega}_{me,k}$ and resistances $\hat{R}_s$ and $\hat{R}_r$. Then, the estimated signals are used to predict the torque $\widetilde{T}_{e,k+1}$, the angular frequency $\widetilde{\omega}_{\overline{\psi}_{s,k+1}}$ and synchronous angle $\widetilde{\theta}_{\overline{\psi}_{s,k+1}}$ at instant $(k+1)T_s$. The values of $\widetilde{\omega}_{\overline{\psi}_{s,k+1}}$ and $\widetilde{\theta}_{\overline{\psi}_{s,k+1}}$ are used besides the power references $P^{*}_{s,k+1}$&$Q^{*}_{s,k+1}$ to calculate the torque and rotor flux reference values ($T^{*}_{e,k+1}$& $\left|\psi^{*}_{r,k+1}\right|$). Finally, the reference torque is compared with the predicted torque value and the error is fed to the designed PI torque adaptor to get the reference power angle δ^{*}_{k+1} which is then added to the angle $\widetilde{\theta}_{\overline{\psi}_{s,k+1}}$ to get the rotor flux angle through which the α-β reference components of the flux ($\psi^{*}_{\alpha r,k+1}$, $\psi^{*}_{\beta r,k+1}$) are obtained and used by the cost function (67). The designed function is then used to select and apply the optimal voltages that achieve the minimum error between the reference and observed flux quantities.

7. Test results

7.1. Testing with PTC

To examine the validity of the proposed sensorless PPFC, extensive tests are made using the Matlab/Simulink. Firstly the DFIG dynamics are evaluated with the traditional PTC considering the designed backstepping observer. The first set of tests is applied for a sinusoidal wind speed variation without exceeding the nominal wind speed as seen in Fig. 10. Meanwhile, the second test is applied when the speed exceeds its nominal value, so that the validity of the MPPT algorithm can be verified. The results for the PTC technique are firstly illustrated as shown in Figs. 11–13 which introduce the calculated values of active and reactive powers, the encounter torque and the rotor flux variation. It can be seen that the active power and the torque are following effectively the wind speed variation; meanwhile the reactive power holds its value to zero as specified by its reference in order to maintain a unity pf. The main notice on these illustrations is the accompanied oscillations which is the main deficiency of the PTC technique. Figs. 14a and 14b show the actual and estimated rotor speed of the DFIGand their relevant estimation error, respectively. It can be shown that the actual rotor speed tracks precisely the wind variation. Figs. 15a and 15b and Figs. 16a and 16b show the observed and actual values of rotor flux components and the observation errors, through which the precision of observation can be fairly examined. The robustness of the designed observer is verified through considering a mismatch in stator resistance of 1.5 times at time $t = 1$ s, and another mismatch in rotor resistance of 1.5 times the value at time $t = 3$ s as presented in Figs. 17a and 17b and Figs. 18a and 18b. From these two figures it is confirmed that the observer is capable of tracking the change of parameters with minimum deviation which consequently enhances the system response under uncertainties.

Figs. 19a and 19b show the actual and observed rotor position and the developed error, from which it is ensured that the observer accomplishes its task with high performance. The correct observation of the position is a vital task for the control system as the position is used to transfer between the various co-ordinates. To present a definite view of the PTC control behavior, Figs. 20–23 visualize the detailed torque variation, detailed rotor flux change, the cost function values and the change in voltage index, respectively. From these illustrations, it is ensured that the problem of ripples is common with the PTC and which inevitably must be handled in order to prevent the generator shaft from the torque oscillations effect. To analyze the ripples behavior with the PTC, the THD is measured for the stator and rotor currents. Figs. 24 and 25 show the FFT spectrums for the α-β current components. The statistics of the FFT analysis are given in Table 1. The waveforms of stator and rotor currents are also presented in Fig. 26(a,b).

7.2. Testing with designed PPFC

In this test, the performance of the designed sensorless PPFC is analyzed for the same conditions considered with the PTC approach. Fig. 27 shows the wind speed variation; meanwhile Figs. 28–30 illustrate the behaviors of the generated power, torque and rotor flux in turn. In comparison with the values obtained with the PTC, the ripples content with the PPFC is effectively reduced which approves the advantage of the designed controller. Moreover, the calculated values track the wind speed change in an appropriate way which reveals the validness of the designed wind energy conversion system. The observer's performance is also tested with the PPFC approach and this can be noticed in Figs. 31a and 31b, Figs. 32a and 32b, Figs. 33a and 33b which configure the real and observer values of shaft speed and rotor flux α-β components and their relevant deviations. Also Figs. 34a, 34b, 35a, 35b, 36a and 36b present the actual and estimated stator and rotor resistances and the rotor position, respectively. From these illustrations, it is obvious that the designed observer exhibits a robust behavior in observing the uncertainties (change in resistances), which consequently makes the system more stable.

To have a zoomed view on the dynamics of the PPFC, samples of torque and flux variations are presented in Figs. 37 and 38. It is very clear that the torque and flux deviations are effectively constrained in comparison with Figs. 20 and 21. Moreover, the calculated minimization function values are presented in Fig. 39 and it is followed by the voltage index change in Fig. 40.

The FFT spectrums for the stator and rotor currents are also presented in Figs. 41 and 42, which report a reduced THD percentage obtained with the designed PPFC in contrast with the obtained values with the PTC procedure. A numerical investigation for the THD is reported in Table 2. Finally, the profiles of the currents are presented in Fig. 43(a,b) which exhibit lower harmonics in relevant to the PTC.

7.3. Testing the MPPT capability with PTC and PPFC

Both control algorithms (PTC and designed PPFC) are tested when the wind speed exceeds its nominal value (11 m/s). This is to check the capability of the MPPT on keeping the maximum extraction of the wind power. The results are introduced in a form of comparison between the two control systems. Fig. 44 shows the wind speed dynamics, while Fig. 45(a,b) show the observed and real shaft speed and its related observation error. Figs. 46–49 illustrate the profiles of generated power, torque and rotor flux under the two control procedures. From these results, it is confirmed that the MPPT is capable to achieve maximum peak power tracking; in addition, the improved dynamics of the DFIG are confirmed with the designed PPFC compared with its behavior under traditional PTC scheme.

The comparative study is also performed via evaluating the accomplished commutations and switching frequencies of the two controllers and the results are numerically presented in Table 3. Through these statistics, it is realized that the designed PPFC presents lower computation burden than the PTC and this is expected due to the simple form of the function (67) used by the

Table 1
THD values for stator and rotor current spectrums with PTC.

Stator current spectrums		Rotor current spectrums	
$i_{\alpha s}$	$i_{\beta s}$	$i_{\alpha r}$	$i_{\beta r}$
Fundamental frequency (50 Hz)		Fundamental frequency (17.25 Hz)	
Fundamental (1514.91 A) THD = 1.73%	Fundamental (1493.54 A) THD = 2.15%	Fundamental (1528.29 A) THD = 0.62%	Fundamental (1513.67 A) THD = 0.60%

Table 2
THD values for stator and rotor current spectrums with PPFC.

Stator current spectrums		Rotor current spectrums	
$i_{\alpha s}$	$i_{\beta s}$	$i_{\alpha r}$	$i_{\beta r}$
Fundamental frequency (50 Hz)		Fundamental frequency (17.25 Hz)	
Fundamental (1505.82 A) THD = 0.74%	Fundamental (1506.82 A) THD= 0.77%	Fundamental (1529.07 A) THD= 0.52%	Fundamental (1518.517 A) THD= 0.41%

Table 3
Commutations and switching frequencies.

PTC		PPFC	
Commutation	Switching frequency	Commutation	Switching frequency
10640	1.77 KHz	6897	1.15 KHz

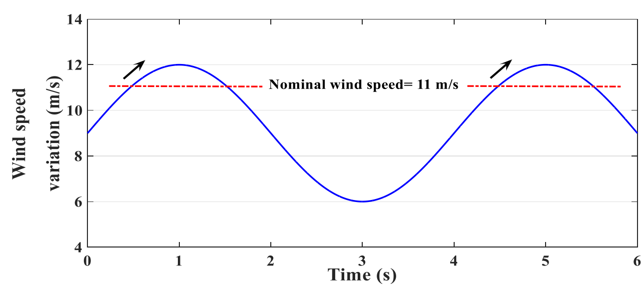

Fig. 44. Wind speed profile.

PPFC. All of this contributes effectively in limiting the switching frequencies and losses as well.

8. Conclusion

The paper introduced an enhanced polar predictive flux control (PPFC) for a sensorless wind driven DFIG. The design of the intended scheme is described in details clarifying each part with its mathematical model. The PPFC approach is considered as a better alternate to the well-known PTC approach with the advantages of limited ripples, low computation capacity and low switching frequency. To elevate the system's stability against irregularities such as parameters' change, a dynamical observer is constructed using the back-stepping methodology in order to track the change in parameters and provide an accurate estimation of the required variables. The appropriateness of the designed controller is tested for a varying wind speed profile considering the operation below nominal speed and when the nominal value is exceeded as well. The designed MPPT strategy approved its ability under the case of exceeding the nominal wind. The obtained results also report the improved system dynamics under the PPFC in comparison with the PTC. In addition, the designed observer proved its fitness in the accurate observation of the variables even under uncertainties.

Funding statement

This publication was made possible by Qatar University Collaborative Research grant # [QUCG-CENG-21/22-1] from the Qatar

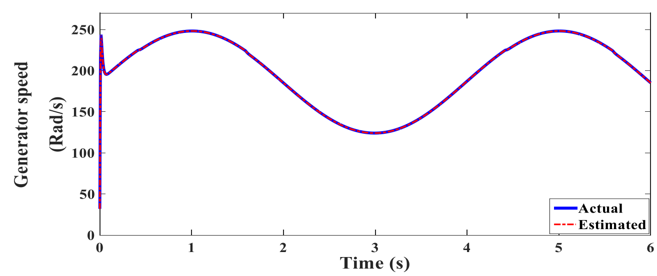

Fig. 45. Generator shaft speed.

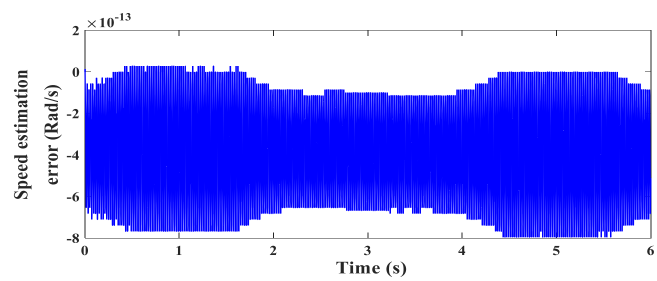

Fig. 46. Observation error of shaft speed.

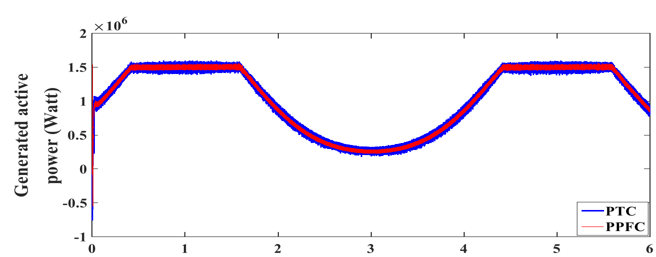

Fig. 47. DFIG power with the two control procedures.

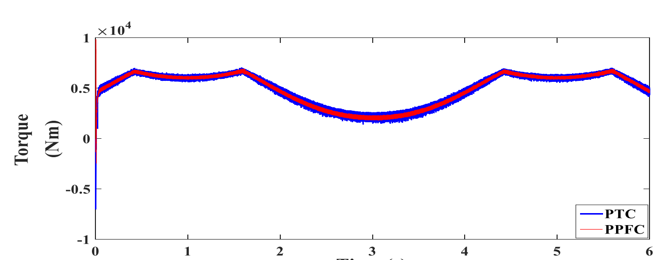

Fig. 48. DFIG torque with the two control procedures.

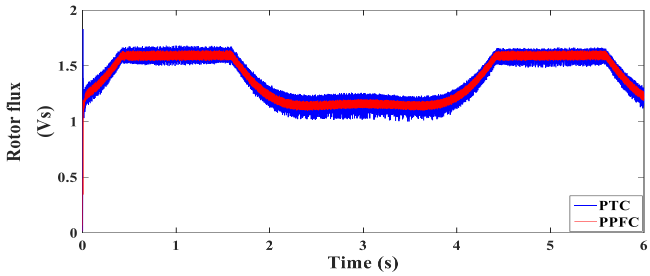

Fig. 49. Rotor flux with the two control procedures.

Table 4
DFIG's Data.

Parameters	Value
Rated power	1.5e6 W
R_s	70 mΩ
R_r	87 mΩ
L_s	16.25 mH
L_r	16.3 mH
Lm	16 mH
p	3
J_g	0.3125 Kg m^2
$U_{sn(\text{nominalstatorvoltage})}$	380 v
Stator frequency	50 Hz

Table 5
Wind turbine Data.

Parameters	Value
Rated power	1.5e6 W
r (Blade radius)	35.25 m
J_t	1000 Kg m^2
$C_{p,max}$	0.51
λ_{opt}	8.1
G (gear ratio)	90

University. The statements made herein are solely the responsibility of the authors.

The open access charges are paid by the Qatar National Library, Doha, Qatar.

CRediT authorship contribution statement

Mahmoud A. Mossa: Conceptualization, Methodology, Validation, Writing – original draft, Supervision. **Hamdi Echeikh:** Data curation, Writing – original draft, Software, Visualization. **Atif Iqbal:** Investigation, Supervision, Writing – review & editing, Formal analysis.

Declaration of competing interest

The authors declare that they have no known competing financial interests or personal relationships that could have appeared to influence the work reported in this paper.

Appendix

See Tables 4 and 5.

References

Abad, G., Rodriguez, M.Á., Poza, J., 2008. Two-level VSC based predictive direct torque control of the doubly fed induction machine with reduced torque and flux ripples at low constant switching frequency. IEEE Trans. Power Electron. 23 (3), 1050–1061.

Ajabi-Farshbaf, R., Azizian, M.R., Eslampanah, V., 2017. A reduced-order observer based on stator flux estimation with straightforward parameter identification for sensorless control of DFIGs. Turkish J. Elect. Eng. Comput. Sci. 25, 3645–3659.

Bhattarai, R., Gurung, N., Ghosh, S., Kamalasadan, S., 2018a. Parametrically robust dynamic speed estimation-based control for doubly fed induction generator. IEEE Trans. Ind. Appl. 54 (6), 6529–6542.

Bhattarai, R., Gurung, N., Thakallapelli, A., Kamalasadan, S., 2018b. Reducedorder state observer-based feedback control methodologies for doubly fed induction machine. IEEE Trans. Ind. Appl. 54 (3), 2845–2856.

Carroll, J., McDonald, A., McMillan, D., 2015. Reliability comparison of wind turbines with DFIG and PMG drive trains. IEEE Trans. Energy Convers. 30 (2), 663–670.

Castelli-Dezza, F., Iacchetti, M.F., Perini, R., 2013. An observer for sensorless DFIM drives based on the natural fifth harmonic of the line voltage, without stator current measurement. IEEE Trans. Ind. Electron. 60 (10), 4301–4309.

Chishti, F., Murshid, S., Singh, B., 2019. Development of wind and solar based AC microgrid with power quality improvement for local nonlinear load using MLMS. IEEE Trans. Ind. Appl. 55 (6), 7134–7145.

Cruz, S.M.A., Marques, G.D., Gonçalves, P.F.C., Iacchetti, M.F., 2018. Predictive torque and rotor flux control of a DFIG-DC system for torque ripple compensation and loss minimization. IEEE Trans. Ind. Electron. 65 (12), 9301–9310.

Davari, S.A., Arab Khburi, D., 2015. Voltage model observer based encoderless predictive control of DFIG for wind tubine applications. In: The 6th Power Electronics, Drive Systems & Technologies Conference, PEDSTC2015, Tehran, pp. 603–608.

Davari, S.A., Nekoukar, V., Garcia, C., Rodriguez, J., 2021. Online weighting factor optimization by simplified simulated annealing for finite set predictive control. IEEE Trans. Ind. Inf. 17 (1), 31–40.

Dezza, F.C., Foglia, G., Iacchetti, M.F., Perini, R., 2012. An MRAS observer for sensorless DFIM drives with direct estimation of the torque and flux rotor current components. IEEE Trans. Power Electron. 27 (5), 2576–2584.

Du, E., et al., 2018. The role of concentrating solar power toward high renewable energy penetrated power systems. IEEE Trans. Power Syst. 33 (6), 6630–6641.

Gaamouche, R., Redouane, A., harraki, I. El, Belhorma, B., El hasnaoui, A., 2020. Optimal feedback control of nonlinear variable-speed marine current turbine using a two-mass model. J. Marine. Sci. Appl. 19, 83–95.

Geng, H., Xu, D., Wu, B., Huang, W., 2011. Direct voltage control for a stand-alone wind-driven self-excited induction generator with improved power quality. IEEE Trans. Power Electron. 26 (8), 2358–2368.

Gomez, L.A.G., Lourenço, L.F.N., Grilo, A.P., Salles, M.B.C., Meegahapola, L., Filho, A.J.S., 2020. Primary frequency response of microgrid using doubly fed induction generator with finite control set model predictive control plus droop control and storage system. IEEE Access 8, 189298-189312.

Han, Y., Kim, S., Ha, J., Lee, W., 2013. A doubly fed induction generator controlled in single-sided grid connection for wind turbines. IEEE Trans. Energy Convers. 28 (2), 413–424.

Holtz, J., 2006. Sensorless control of induction machines—With or without signal injection. IEEE Trans. Ind. Electron. 53 (1), 7–30.

Hu, J., Zhu, J., Dorrell, D.G., 2015. Predictive direct power control of doubly fed induction generators under unbalanced grid voltage conditions for power quality improvement. IEEE Trans. Sustain. Energy 6 (3), 943–950.

Iacchetti, M.F., Marques, G.D., Perini, R., 2015. A scheme for the power control in a DFIG connected to a DC bus via a diode rectifier. IEEE Trans. Power Electron. 30 (3), 1286–1296.

Kanjiya, P., Ambati, B.B., Khadkikar, V., 2014. A novel fault-tolerant DFIG-based wind energy conversion system for seamless operation during grid faults. IEEE Trans. Power Syst. 29 (3), 1296–1305.

Karakasis, N., Tsioumas, E., Jabbour, N., Bazzi, A.M., Mademlis, C., 2019. Optimal efficiency control in a wind system with doubly fed induction generator. IEEE Trans. Power Electron. 34 (1), 356–368.

Karthikeyan, A., Nagamani, C., Ray Chaudhury, A.B., Ilango, G.S., 2012. Implicit position and speed estimation algorithm without the flux computation for the rotor side control of doubly fed induction motor drive. IET Electr. Power Appl. 6 (4), 243–252.

Koraki, D., Strunz, K., 2018. Wind and solar power integration in electricity markets and distribution networks through service-centric virtual power plants. IEEE Trans. Power Syst. 33 (1), 473–485.

Krstić, M., Kanellakopoulos, I., Kokotović, P., 1995. Nonlinear and Adaptive Control Design. Wiley, Hoboken, NJ, USA.

Kumar, R., Das, S., 2017. MRAS-based speed estimation of grid-connected doubly fed induction machine drive. IET Power Electron. 10 (7), 726–737.

Kumar, K., Ramesh Babu, N., Prabhu, K.R., 2017. Design and analysis of RBFN-based single MPPT controller for hybrid solar and wind energy system. IEEE Access 5, 15308–15317.

Li, D., Cai, W., Li, P., Xue, S., Song, Y., Chen, H., 2018. Dynamic modeling and controller design for a novel front-end speed regulation (FESR) wind turbine. IEEE Trans. Power Electron. 33 (5), 4073–4087.

Marques, G.D., Sousa, D.M., 2011. Air-gap-power-vector-based sensorless method for DFIG control without flux estimator. IEEE Trans. Ind. Electron. 58 (10), 4717–4726.

Marques, G.D., Sousa, D.M., 2012. Stator flux active damping methods for field-oriented doubly fed induction generator. IEEE Trans. Energy Convers. 27 (3), 799–806.

Marques, G.D., Sousa, D.M., 2013. Sensorless direct slip position estimator of a DFIM based on the air gap pq vector-sensitivity study. IEEE Trans. Ind. Electron. 60 (6), 2442–2450.

Marques, G.D., Sousa, D.M., Iacchetti, M.F., 2013. An open-loop sensorless slip position estimator of a DFIM based on air-gap active power calculations—sensitivity study. IEEE Trans. Energy Convers. 28 (4), 959–968.

Mendis, N., Muttaqi, K.M., Sayeef, S., Perera, S., 2012. Standalone operation of wind turbine-based variable speed generators with maximum power extraction capability. IEEE Trans. Energy Convers. 27 (4), 822–834.

Mohammadi, J., Vaez-Zadeh, S., Afsharnia, S., Daryabeigi, E., 2014. A combined vector and direct power control for DFIG-based wind turbines. IEEE Trans. Sustain. Energy 5 (3), 767–775.

Mohseni, M., Islam, S.M., Masoum, M.A.S., 2011. Enhanced hysteresis-based current regulators in vector control of DFIG wind turbines. IEEE Trans. Power Electron. 26 (1), 223–234.

Mokhtari Vayeghan, M., Davari, S.A., 2017. Torque ripple reduction of DFIG by a new and robust predictive torque control method. IET Renew. Power Gener. 11 (11), 1345–1352.

Mondal, S., Kastha, D., 2015. Improved direct torque and reactive power control of a matrix-converter-fed grid-connected doubly fed induction generator. IEEE Trans. Ind. Electron. 62 (12), 7590–7598.

Morawiec, M., 2015. Z type observer backstepping for induction machines. IEEE Trans. Ind. Electron. 62 (4), 2090–2103.

Nayanar, V., Kumaresan, N., Ammasai Gounden, N., 2016. A single-sensor-based MPPT controller for wind-driven induction generators supplying DC microgrid. IEEE Trans. Power Electron. 31 (2), 1161–1172.

Ni, R., Xu, D., Blaabjerg, F., Lu, K., Wang, G., Zhang, G., 2017. Square-wave voltage injection algorithm for PMSM position sensorless control with high robustness to voltage errors. IEEE Trans. Power Electron. 32 (7), 5425–5437.

Polinder, H., Ferreira, J.A., Jensen, B.B., Abrahamsen, A.B., Atallah, K., McMahon, R.A., 2013. Trends in wind turbine generator systems. IEEE J. Emerg. Sel. Top. Power Electron. 1 (3), 174–185.

Puchalapalli, S., Tiwari, S.K., Singh, B., Goel, P.K., 2020. A microgrid based on wind-driven DFIG, DG, and solar PV array for optimal fuel consumption. IEEE Trans. Ind. Appl. 56 (5), 4689–4699.

Pulgar-Painemal, H., 2019. Enforcement of current limits in DFIG-based wind turbine dynamic models through capability curve. IEEE Trans. Sustain. Energy 10 (1), 318–320.

Rahimi, M., Parniani, M., 2010. Transient performance improvement of wind turbines with doubly fed induction generators using nonlinear control strategy. IEEE Trans. Energy Convers. 25 (2), 514–525.

Sguarezi Filho, A.J., Filho, E.R., 2012. Model-based predictive control applied to the doubly-fed induction generator direct power control. IEEE Trans. Sustain. Energy 3 (3), 398–406.

Soliman, M., Malik, O.P., Westwick, D.T., 2011. Multiple model predictive control for wind turbines with doubly fed induction generators. IEEE Trans. Sustain. Energy 2 (3), 215–225.

Stojić, D., Milinković, M., Veinović, S., Klasnić, I., 2015. Improved stator flux estimator for speed sensorless induction motor drives. IEEE Trans. Power Electron. 30 (4), 2363–2371.

Sun, W., Yu, Y., Wang, G., Li, B., Xu, D., 2016. Design method of adaptive full order observer with or without estimated flux error in speed estimation algorithm. IEEE Trans. Power Electron. 31 (3), 2609–2626.

Taibi, F., Benzineb, O., Tadjine, M., Boucherit, M.S., Benbouzid, M.E.H., 2014. Hybrid sliding mode control of DFIG with MPPT using three multicellular converters. IFAC Proc. Vol. 47 (3), 11659–11666.

Trabelsi, R., Khedher, A., Mimouni, M.F., M'Sahli, F., 2012. Backstepping control for an induction motor using an adaptive sliding rotor-flux observer. Electr. Power Syst. Res. 93, 1.

Wang, X., Sun, D., Zhu, Z.Q., 2017. Resonant-based backstepping direct power control strategy for DFIG under both balanced and unbalanced grid conditions. IEEE Trans. Ind. Appl. 53 (5), 4821–4830.

Wei, X., Cheng, M., Zhu, J., Yang, H., Luo, R., 2019. Finite-set model predictive power control of brushless doubly fed twin stator induction generator. IEEE Trans. Power Electron. 34 (3), 2300–2311.

Williamson, K.H., Gunderson, R.P., Hamblin, G.M., Gallup, D.L., Kitz, K., 2001. Geothermal power technology. Proc. IEEE 89 (12), 1783–1792.

Xiahou, K., Li, M.S., Liu, Y., Wu, Q.H., 2018. Sensor fault tolerance enhancement of DFIG-WTs via perturbation observer-based DPC and two-stage Kalman filters. IEEE Trans. Energy Convers. 33 (2), 483–495.

Xiahou, K., Liu, Y., Wang, L., Li, M.S., Wu, Q.H., 2019. Switching fault-tolerant control for DFIG-based wind turbines with rotor and stator current sensor faults. IEEE Access 7, 103390-103403.

Xiong, P., Sun, D., 2016. Backstepping-based DPC strategy of a wind turbine-driven DFIG under normal and harmonic grid voltage. IEEE Trans. Power Electron. 31 (6), 4216–4225.

Yin, Z., Li, G., Zhang, Y., Liu, J., 2019. Symmetric-strong-tracking-extended Kalman-filter-based sensorless control of induction motor drives for modeling error reduction. IEEE Trans. Ind. Inf. 15 (2), 650–662.

You, J., Wu, W., Wang, Y., 2018. An adaptive luenberger observer for speed sensorless estimation of induction machines. In: Proc. Annu. Amer. Control Conf., pp. 307–312.

Zarei, M.E., Veganzones Nicolás, C., Rodríguez Arribas, J., 2017. Improved predictive direct power control of doubly fed induction generator during unbalanced grid voltage based on four vectors. IEEE J. Emerg. Sel. Top. Power Electron. 5 (2), 695–707.

Zebirate, S., Chaker, A., Feliachi, A., 2014. Neural predictive control of a doubly fed induction generator. Int. Rev. Model. Simul. (IREMOS) 7 (5), 782–790.

Zeng, B., Zhang, J., Yang, X., Wang, J., Dong, J., Zhang, Y., 2014. Integrated planning for transition to low-carbon distribution system with renewable energy generation and demand response. IEEE Trans. Power Syst. 29 (3), 1153–1165.

Zhang, Y., Jiao, J., Xu, D., Jiang, D., Wang, Z., Tong, C., 2020a. Model predictive direct power control of doubly fed induction generators under balanced and unbalanced network conditions. IEEE Trans. Ind. Appl. 56 (1), 771–786.

Zhang, Y., Jiao, J., Xu, D., Jiang, D., Wang, Z., Tong, C., 2020b. Model predictive direct power control of doubly fed induction generators under balanced and unbalanced network conditions. IEEE Trans. Ind. Appl. 56 (1), 771–786.

Zhang, G., Wang, G., Xu, D., Zhao, N., 2016. ADALINE-network-based PLL for position sensorless interior permanent magnet synchronous motor drives. Power Electron. 31, 1450–1460.

Zhang, Z., Zhao, Y., Qiao, W., Qu, L., 2014. A space-vector-modulated sensorless direct-torque control for direct-drive PMSG wind turbines. IEEE Trans. Ind. Appl. 50 (4), 2331–2341.